nature materials

ARTICLES

https://doi.org/10.1038/s41563-020-00807-1



# Observation of fluctuation-mediated picosecond nucleation of a topological phase

Felix Büttner[1,13,15]✉, Bastian Pfau[2,15]✉, Marie Böttcher[3], Michael Schneider[2], Giuseppe Mercurio[4], Christian M. Günther[5,6], Piet Hessing[2], Christopher Klose[2], Angela Wittmann[1], Kathinka Gerlinger[2], Lisa-Marie Kern[2], Christian Strüber[2], Clemens von Korff Schmising[2], Josefin Fuchs[2], Dieter Engel[2], Alexandra Churikova[1], Siying Huang[1], Daniel Suzuki[1], Ivan Lemesh[1], Mantao Huang[1], Lucas Caretta[1], David Weder[2], John H. Gaida[7], Marcel Möller[7], Tyler R. Harvey[7], Sergey Zayko[7], Kai Bagschik[8], Robert Carley[4], Laurent Mercadier[4], Justine Schlappa[4], Alexander Yaroslavtsev[4], Loïc Le Guyarder[4], Natalia Gerasimova[4], Andreas Scherz[4], Carsten Deiter[4], Rafael Gort[4], David Hickin[4], Jun Zhu[4], Monica Turcato[4], David Lomidze[4], Florian Erdinger[9], Andrea Castoldi[10,11], Stefano Maffessanti[8], Matteo Porro[4], Andrey Samartsev[4], Jairo Sinova[3], Claus Ropers[7], Johan H. Mentink[12], Bertrand Dupé[3,14], Geoffrey S. D. Beach[1] and Stefan Eisebitt[2,6]

**Topological states of matter exhibit fascinating physics combined with an intrinsic stability. A key challenge is the fast creation of topological phases, which requires massive reorientation of charge or spin degrees of freedom. Here we report the picosecond emergence of an extended topological phase that comprises many magnetic skyrmions. The nucleation of this phase, followed in real time via single-shot soft X-ray scattering after infrared laser excitation, is mediated by a transient topological fluctuation state. This state is enabled by the presence of a time-reversal symmetry-breaking perpendicular magnetic field and exists for less than 300 ps. Atomistic simulations indicate that the fluctuation state largely reduces the topological energy barrier and thereby enables the observed rapid and homogeneous nucleation of the skyrmion phase. These observations provide fundamental insights into the nature of topological phase transitions, and suggest a path towards ultrafast topological switching in a wide variety of materials through intermediate fluctuating states.**

Femtosecond laser pulses can induce phase transitions and unexpected transient states of matter on ultrafast timescales. Examples range from crystallographic phase transitions[1] over charge ordering[2,3] to transitions into hidden quantum phases[4]. If the transitions involve spontaneous symmetry breaking and, moreover, proceed faster than the characteristic quasiparticles can propagate across the transition volume, causality requires the formation of grain-boundary-type topological defects. In non-topological materials, the final-state density of such defects is well understood. For example, the formation of vortices in superfluids and superconductors is described by the Kibble–Zurek mechanism (KZM)[5], which links the defect density to a power law of the cooling rate through the second-order phase transition. Moreover, phase transitions exist between bound and free topological states, as formulated in the Berezinskii–Kosterlitz–Thouless theory[6], which, however, preserve the topological invariants. Phase transitions that involve net topological switching, here referred to as global topological phase transitions[7], are conceptually different and much less understood. In particular, although the annihilation dynamics of a topological state was recently reported[8], the formation of topological phases has been observed only under quasi-static conditions[9–13], which leaves the mechanism and speed of such phase transitions largely unexplored.

Perpendicular magnetic thin-film ferromagnets are ideal candidates to investigate the dynamics of global topological phase transitions. First, these materials respond strongly to femtosecond laser pulses by ultrafast demagnetization[14,15] and all-optical switching[16], even though the mechanism of the latter process is still under debate. Second, many perpendicular magnetic ferromagnets exhibit a topological skyrmion ground state in a finite range of externally applied fields[17–22]. The intrinsic stability of such a skyrmion phase arises at room temperature primarily from non-local stray-field interactions and the Dzyaloshinskii–Moriya interaction (DMI) can additionally enforce this stability and determine the skyrmion chirality. The skyrmion phase is topologically protected and therefore often hidden during adiabatic field cycling[17,20] (Fig. 1a). Instead, it can be accessed by spatially inhomogeneous or dynamical excitations[20,23,24], which

[1]Department of Materials Science and Engineering, Massachusetts Institute of Technology, Cambridge, MA, USA. [2]Max-Born-Institut, Berlin, Germany. [3]Institut für Physik, Johannes Gutenberg Universität Mainz, Mainz, Germany. [4]European XFEL, Schenefeld, Germany. [5]Zentraleinrichtung Elektronenmikroskopie (ZELMI), Technische Universität Berlin, Berlin, Germany. [6]Institut für Optik und Atomare Physik, Technische Universität Berlin, Berlin, Germany. [7]4th Physical Institute, University of Göttingen, Göttingen, Germany. [8]Deutsches Elektronen-Synchrotron (DESY), Hamburg, Germany. [9]Institute of Computer Engineering, Heidelberg University, Heidelberg, Germany. [10]Dipartimento di Elettronica, Informazione e Bioingegneria, Politecnico di Milano, Milano, Italy. [11]Istituto Nazionale di Fisica Nucleare, Sezione di Milano, Milano, Italy. [12]Institute for Molecules and Materials, Radboud University, Nijmegen, the Netherlands. [13]Present address: Helmholtz-Zentrum für Materialien und Energie GmbH, Berlin, Germany. [14]Present address: Nanomat/Q-mat/CESAM, Université de Liège, Belgium and Fonds de la Recherche Scientifique (FNRS), Bruxelles, Belgium. [15]These authors contributed equally: Felix Büttner and Bastian Pfau. ✉e-mail: Felix.Buettner@helmholtz-berlin.de; Bastian.Pfau@mbi-berlin.de

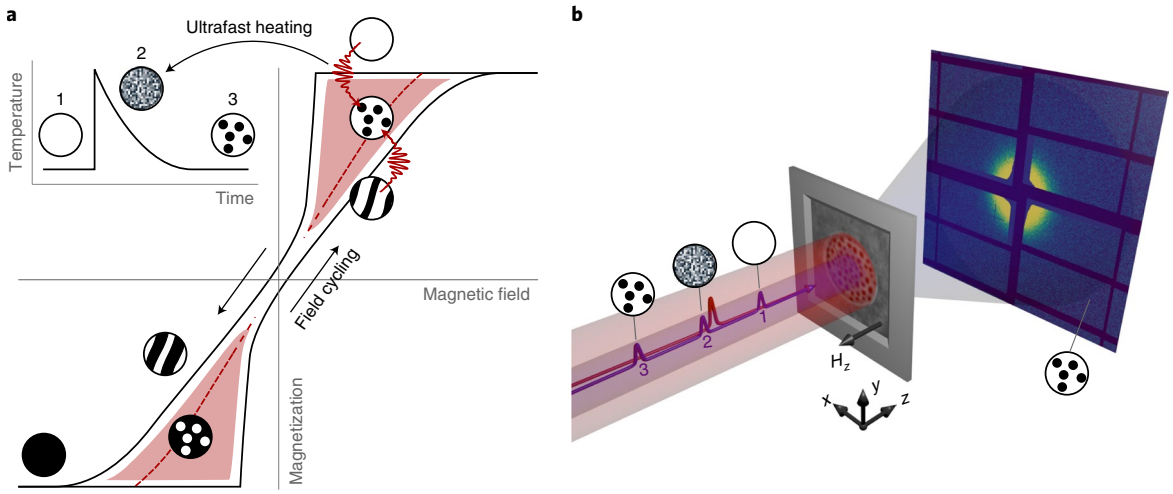


**Fig. 1 | Topological magnetic phase transition mediated by a transient fluctuation state. a**, Typical room-temperature phases of a ferromagnetic thin-film skyrmion material as a function of a perpendicular magnetic field. Field-accessible magnetic phases are indicated by pictographs along the solid black hysteresis curve (homogeneous black or white, uniform down or up, respectively; stripes, stripe domains; circles, skyrmions). The laser-accessible skyrmion phase is located between the hysteresis branches. The dashed red line schematically indicates the average out-of-plane magnetization of the lowest-energy skyrmion texture. Wavy red arrows illustrate phase transitions induced by laser pulses. Inset: the evolution of sample temperature and magnetic states from a uniform state (1) via a fluctuation state (2) to a skyrmion texture (3). **b**, Schematic of the time-resolved detection process. The sample comprises a magnetic multilayer on an X-ray transparent membrane in an out-of-plane magnetic field $H_z$. The sample is exposed to a train of three X-ray pulses and one infrared laser pulse, which has a well-defined delay with respect to the second X-ray pulse. The coherent diffraction of the X-ray pulses is recorded by a camera with a submicrosecond readout speed. The scattering pattern shown here corresponds to a skyrmion state.

include femtosecond laser pulses[12,13]. Owing to the large topological energy barriers, which often exceed 100 times the thermal energy at room temperature[25], it is expected that the transition into the topological phase is governed by rare, heterogeneous switching events followed by domain wall motion dynamics on a nanosecond timescale or slower[12,17].

Here we performed single-shot infrared pump–X-ray probe measurements to follow the topological switching dynamics from a uniform field-polarized state into a dense skyrmion phase in real time (Fig. 1b). The experiment was conducted at the soft X-ray beamline SCS of the European X-ray free-electron laser (XFEL) source, which provides exceptional sensitivity to the process in combination with temporal and reciprocal-space resolution. We discovered that the topological phase transition is essentially completed within 300 ps, much faster even than the simple reorientation of existing stripe domains under similar conditions[26]. The unexpected speed of this transition is enabled by evolution through a transient topological fluctuation state—a state that can be distinguished from non-topological fluctuations[27] by its evolution into stable, homotopological texture. The high speed is additionally attributed to the homogeneous nucleation of skyrmions, analogous to the freezing of supercooled water and the condensation of magnons[27]. We show that the fluctuation state and the skyrmion formation dynamics are in excellent agreement with atomistic spin dynamics simulations, which leads to a detailed microscopic understanding of all-optical topological switching.

## Demonstration of net topological switching

Our study of laser-induced topological phase transitions was based on two related perpendicular magnetic multilayer materials: $Ta(3.6\,nm)/Pt(3.7\,nm)/[Pt(2.7\,nm)/Co_{60}Fe_{20}B_{20}(0.9\,nm)/MgO(1.5\,nm)]_{15}/Pt(2.7\,nm)$ and $Ta(3\,nm)/[Co(0.6\,nm)/Pt(0.8\,nm)]_{15}/Ta(2\,nm)$, which we subsequently refer to as Pt/CoFeB/MgO and Pt/Co, respectively. Both materials feature Pt/Co interfaces with strong spin–orbit coupling that can, in principle, facilitate chiral interactions and host magnetic skyrmions. To demonstrate topological switching in these materials, we followed the procedure illustrated in Fig. 1a and imaged the field- and laser-accessible magnetic phases at room temperature by in-situ X-ray holography (see Methods and Extended Data Figs. 1 and 2 for the experimental details).

Figure 2a shows the results for Pt/CoFeB/MgO. During field cycling, we found topologically trivial uniform or stripe domain states. We found that these field-induced states can be transformed into pure skyrmion states by single femtosecond laser pulses, provided that time-reversal symmetry is broken by an out-of-plane magnetic field or at least by a notable remanent magnetization of the sample (Fig. 2a, top, and Supplementary Section 1). Without such symmetry breaking we observed no skyrmion formation at any laser fluence below the destruction threshold of the material (Fig. 2a, bottom). To demonstrate the topology of the laser-induced magnetic textures, we tracked their spin–orbit torque current-driven motion, as shown in Fig. 2b and Extended Data Fig. 3. We found that all the circular textures moved in the direction of the current and that their trajectories were systematically inclined at an angle to the current axis. This is due to the skyrmion Hall effect[28,29] and confirms that the observed domains are homochiral skyrmions. These results are consistent with Je et al.[13] and establish the behaviour suggested in Fig. 1a for chiral materials.

Similar switching characteristics are found in Pt/Co (Fig. 2c), even though the thickness-averaged chiral interactions are expected to be negligible in this symmetric material. To determine the chirality and topology of laser-induced circular domains in Pt/Co, we employed Lorentz transmission electron microscopy (LTEM) instead of current-driven dynamics due to nominally cancelling spin–orbit torques. Circular domains were nucleated in situ, as described in Methods, and subsequently imaged by LTEM at normal incidence. The LTEM image of the laser-induced state, shown in Fig. 2d, is characterized by a dense arrangement of randomly black and white circles. Unlike the X-ray images, which show the out-of-plane magnetization, LTEM at normal incidence is sensitive to the Bloch in-plane component of domain walls[18,21]. Specifically, a bright (dark) inner ring corresponds to anticlockwise

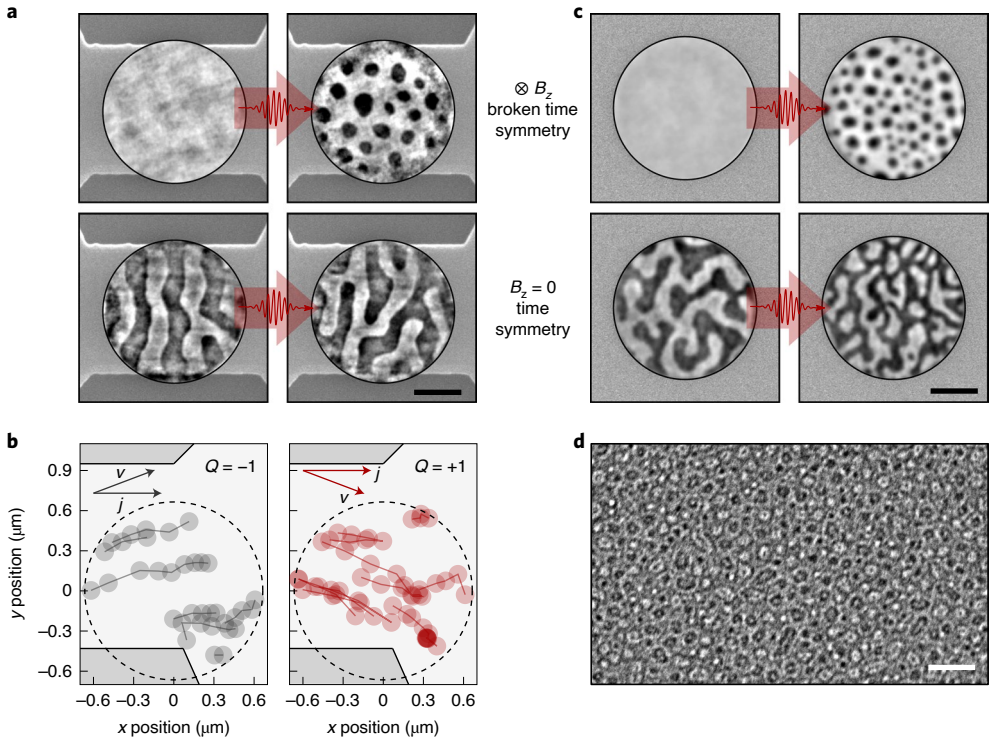


**Fig. 2 | All-optical topological switching in Pt/CoFeB/MgO and Pt/Co. a**, Single-shot laser-induced phase transitions in Pt/CoFeB/MgO at a variable external perpendicular magnetic field following the sequence (1) → (3) illustrated in Fig. 1a at $B_z = 19$ mT (top) and after a.c. out-of-plane demagnetization (bottom). The background shows scanning electron micrographs of the respective samples (see Extended Data Fig. 2 for larger scanning electron micrograph images). The grey contrast of the images in the circles represents the out-of-plane magnetization $m_z$. The switching fluence was 16 mJ cm$^{-2}$. **b**, Trajectories of laser-nucleated skyrmions in Pt/CoFeB/MgO driven by spin–orbit current pulses $j$ in a positive field (37 mT, left) and in a negative magnetic field (−36 mT, right) (see Extended Data Fig. 3 for all the frames). The dark-grey background indicates areas outside the magnetic track. The dashed circle marks our field of view. Full circles correspond to skyrmion positions and the lines connect positions of the same skyrmion in subsequent frames. Position error bars are smaller than the data points. The topology $Q$ is confirmed by the angle of the trajectory $v$ with respect to the current direction $j$. **c**, Same data as in **a**, but for Pt/Co, following the sequence (1) → (3) illustrated in Fig. 1a at $B_z = 41$ mT and a fluence of 17 mJ cm$^{-2}$ (top) after a.c. out-of-plane demagnetization and a fluence of 65 mJ cm$^{-2}$ (bottom). **d**, LTEM of laser-nucleated skyrmions in Pt/Co in a field of 25 mT using the overfocus imaging condition. Bright (dark) contrast inside a circular texture indicates anticlockwise (clockwise) Bloch chirality. Scale bars, 500 nm.

(clockwise) Bloch chirality (a transport of intensity reconstruction of the in-plane spin configuration is shown in Extended Data Fig. 4a). The black and white contrast appears with approximately equal probability. However, this only illustrates that the Bloch chirality, which is not a topological number, is randomly assigned, as expected in this non-chiral material. More importantly, the fact that all the circular features, regardless of colour, exhibit an isotropic LTEM contrast means that the spins rotate exactly once when moving along the domain perimeter. This implies that, even though the material itself is non-chiral and quasistatically generated spin textures are non-topological (Extended Data Figure 4b), all the laser-nucleated spin textures in our image share the same unit topological charge: they are skyrmions.

## Signatures of a dynamical phase transition

Before we studied the dynamics of all-optical topological switching, we performed a systematic scan of the parameter space, from which we found two types of switching: thermally activated reversal and phase-transition-mediated switching. These two regimes are illustrated by the evolution of spin textures after consecutive laser pulses, as shown in Fig. 3a. At low fluences, we observed gradual, probabilistic switching, in which an initially saturated material is first transformed into a stripe domain state by one or a few laser pulses and this stripe domain state gradually evolves into a dense skyrmion texture by $>10^4$ pulses (see Supplementary Section 2 for the images that correspond to Fig. 3a). By contrast, above a sharp critical fluence of ~15 mJ cm$^{-2}$, we deterministically observed pure skyrmion states after just one laser pulse. This abrupt increase of the switching rate points to a critical behaviour, as expected in the vicinity of a (dynamical) phase transition, which we here characterize by the emergence of a global topological charge.

The switching thresholds were similar in both materials (Supplementary Section 3), and the same threshold behaviour was observed whether starting from a uniform or stripe domain state (Fig. 3b). The threshold was independent of the pulse duration for pulses between 250 fs and 10 ps, as demonstrated in Fig. 3b. The density of skyrmions above the fluence threshold was constant (Supplementary Sections 2 and 3). Moreover, the distribution of laser-induced skyrmions, as shown in the inset of Fig. 3a, was characterized by a variance-over-mean of $1.6 \approx 1$, indicative of a shot-noise Poisson distribution with a homogeneous nucleation probability. This contrasts with spin-torque mediated skyrmion nucleation in nominally the same material[24], in which a variance-over-mean of $12.1 \gg 1$ was found in accordance with the fact that spin-torque nucleation relies on extrinsic lateral inhomogeneities to break the symmetry at the point of nucleation[24,30] (see Extended Data Fig. 5 and Supplementary Section 4 for details). Even though the defect density and strength are different for each sample, our observations provide a strong indication that all-optical topological switching is an intrinsic process. Our observations are also in contrast with

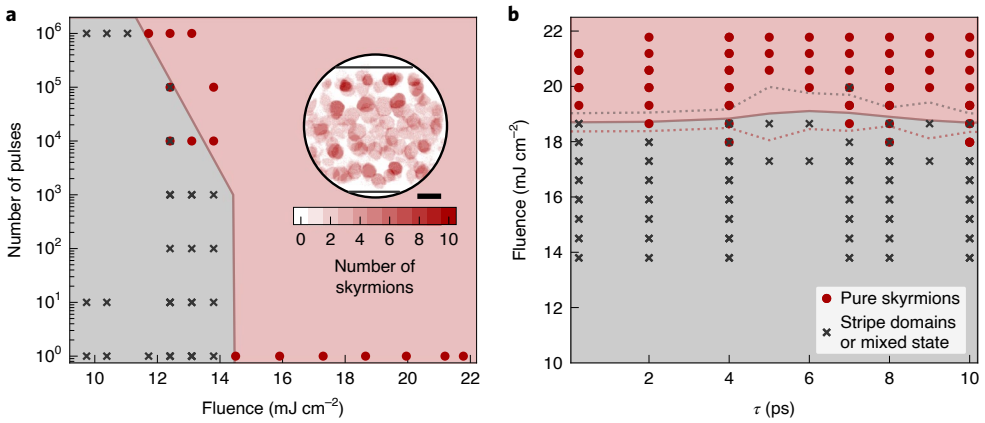


**Fig. 3 | Switching threshold in Pt/CoFeB/MgO as a function of laser pulse number, fluence and duration. a**, Final state as a function of laser fluence and number of laser pulses, starting from a saturated state (for the corresponding real-space images, see Supplementary Fig. 2). Mixed states were observed below ~14.5 mJ cm$^{-2}$, where they gradually transformed into skyrmion arrays by many pulses. As pure skyrmion states we identified patterns of fully enclosed domains with a density that remained constant on subsequent laser exposure. All the data correspond to $\tau = 250$ fs pulses and an applied field of $\mu_0 H_z \approx 10$ mT. The background colour is a guide to the eye. Inset: the integrated distribution of skyrmions in ten patterns obtained by single laser pulses from a stripe domain state. Scale bar, 250 nm. **b**, Final state after one single laser pulse as a function of pulse duration $\tau$ and fluence at $\mu_0 H_z \approx 16$ mT, starting from a stripe domain state. The dashed lines denote the uncertainty interval that separates the high-fluence single-shot skyrmion states from the mixed states observed at lower fluences (s.d.).

findings for B20 materials, in which skyrmion nucleation preferentially takes place at sample edges and magnetic phase boundaries[12]. Unlike topological defect formation in non-topological materials[2,3,31], the pulse-duration independence of the transition suggests that skyrmion formation above the switching threshold relies on neither the demagnetization time nor the relaxation time to the final state.

## Direct observation of picosecond skyrmion formation dynamics

We directly followed the dynamics of the global topological phase transition by pulse-resolved small-angle X-ray scattering (SAXS) measurements at the European XFEL, as illustrated in Fig. 1b. These measurements are sensitive to the amplitude squared of the spatial Fourier transform of the out-of-plane magnetization $m_z(x,y)$. We employed Pt/Co multilayers for a maximum contrast, and chose a field (83 mT; Extended Data Figs. 6 and 7) and fluence (~50 mJ cm$^{-2}$) in a regime in which quasi-static imaging (Fig. 2c and Supplementary Fig. 3) confirms robust switching from a topologically trivial field-polarized state into a pure skyrmion final state. The experiment was conducted in saturate–pump–probe cycles (Supplementary Section 7), in which each cycle started with a field sweep from 263 to 83 mT to prepare the magnetic material in a metastable, uniform initial state, followed by three X-ray pulses and one infrared laser pulse, as illustrated in Fig. 1b and Extended Data Fig. 7. The initial state (Fig. 4a) and final state (Fig. 4c) were recorded at every cycle to confirm that we switched from a saturated state to a skyrmion state. For the experimental details, see Methods and Supplementary Sections 5–8.

The transient-state SAXS patterns were both quantitatively and qualitatively different from the final state scattering, as illustrated in Fig. 4b. On a timescale of up to ~100 ps after the laser pulse, we observed weak and almost perfectly uniform scattering. This corresponds to a disordered state characterized by an almost equal distribution of all length scales, similar to recent observations in GdFeCo (ref. [27]), but in our case this led to the formation of a stable texture.

The $q$-integrated instantaneous intensity $I(t)$ is shown in Fig. 4d. This quantity was calculated by (1) summing all the detector pixels between $q_{\min} = 0.02\,\mathrm{nm}^{-1}$ and $q_{\max} \approx 0.155\,\mathrm{nm}^{-1}$ (Methods), (2) normalizing this sum to the incident intensity and (3) dividing the result by the average of all the final state intensities (also calculated using steps (1) and (2)). $I(t)$ is proportional to the coherent sum $\int_{q_{\min}}^{q_{\max}} \mathrm{d}q \left| F\left(\sum_{i=1}^{15} m_{z,i}\right)\right|^2$ of the lateral Fourier transform of $m_z$ in all layers $i$ and therefore a sensitive measure of both the formation of texture in the detected $q$ range and of the ferromagnetic alignment between the layers. The measured $I(t)$ exhibited a monotonic increase after the laser excitation. The growth rate was initially small, peaks at $t = (90 \pm 40)$ ps, and subsequently decayed exponentially with a time constant of $56 \pm 9$ ps (errors are s.d.; Methods and Supplementary Section 9). The integrated intensity reached 80% of the final state intensity at 300 ps after the laser pulse. Such a strong scattering, irrespective of the missing low-$q$ part, can only occur if $m_{z,i}$ is the same in $\sqrt{0.8} = 90\%$ of all layers. As the out-of-plane direction is the direction of weakest coupling in our sample, we conclude that 300 ps is an upper bound for the timescale at which ferromagnetic order is restored.

Figure 4e shows the full momentum $q$ and time $t$ resolved scattering $I(q,t)$, for which we averaged the azimuthally isotropic scattering data along the azimuth angle (see Extended Data Fig. 8 for individual $I(q)$ plots). At around 100 ps the scattering became strong enough for quantitative analysis. Here we could already observe a weak peak, which corresponded to small skyrmions or reversed domain nuclei that later developed into skyrmions. From the peak position and the decay at its high $q$ shoulder we extracted the correlation length (the average distance of skyrmion nuclei) and an estimate for the nuclei size, respectively. Details of this analysis are discussed in the Methods and Supplementary Section 10 and the fits are shown in Extended Data Figs. 9 and 10. The time dependence of the correlation length and the skyrmion diameter are plotted in Fig. 4d. Both length scales exhibit a rapid increase that initially coincides with an increase of total intensity. However, although the total intensity saturates at 300 ps, both the skyrmion size and their average distance continued to increase even at the longest measured delay, 1 ns. As the average $m_z$ does not change after 300 ps, the increase of scattering at low $q$ due to skyrmion growth must be compensated by a reduction of high-$q$ spin fluctuations. This observation indicates that skyrmions grow by condensation

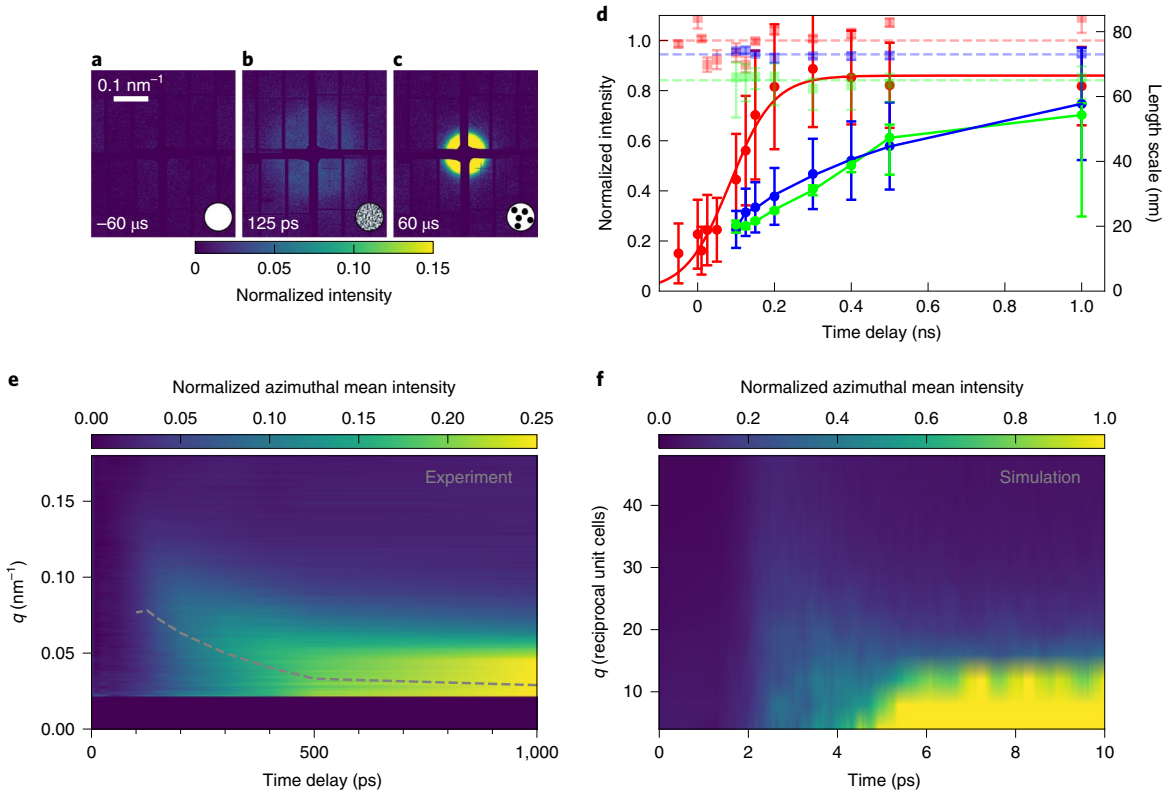


**Fig. 4 | Time-resolved observation of the topological phase transition. a–c**, Example SAXS patterns before (**a**), during (**b**) and after (**c**) the laser-induced nucleation dynamics (cropped to the central region). The delay between the respective X-ray pulse and the infrared pulse is indicated. Insets: corresponding real-space spin textures. **d**, Normalized total scattered intensity (red), correlation length × 0.25 (green) and skyrmion diameter (blue) as a function of time delay (circular data points). Square data points show the control measurements of the final state recorded for each pump–probe shot. The solid red line is a fit to a logistic function (see Methods for details). Other solid lines are guides to the eye. Dashed lines represent the average of the final state values. Error bars represent the estimated s.e.m. Error bars for intensity were estimated by variation of the upper integration limit (Methods). Other error bars are fit and model errors (see Supplementary Section 10 for details). **e**, $q$-dependent scattering (azimuthal average) of the transient state as a function of pump–probe delay. The intensity $I$ at larger $q$ values corresponds to higher spatial gradients in real space. The dashed line indicates the fitted peak positions. This line only seems to be at the low $q$ side of the maximum due to the broad and asymmetric shape of $I(q)$ at small time delays. **f**, Simulated $q$-dependent scattering, which corresponds to the data shown in Fig. 5.

of high-energy magnons[27] and skyrmion coalescence, and not by classical domain-wall motion, which contributes to the exceptional high speed of this transition.

## Atomistic simulations of topological switching dynamics

We employed atomistic simulations to qualitatively understand the intrinsic skyrmion nucleation dynamics. Atomistic simulations are the established approach to simulate ultrafast magnetization dynamics because they accurately account for non-equilibrium phenomena and because they can describe the large angles between neighbouring spins that typically characterize high-temperature states. To reduce the otherwise overwhelming computational complexity, we considered a simplified model system of a magnetic monolayer and took into account the Heisenberg exchange interaction, the DMI, the easy-axis anisotropy and the applied field (see Methods and Lemesh et al.[32] for more details). The equilibrium phase diagram of our model system, shown in Fig. 5a, exhibits long-ranged ordered spin-spiral and uniform ferromagnetic states at low temperatures. Above temperature $T_1$, fluctuations turned the long-ranged ordered phases into a short-ranged ordered skyrmion phase, which is known as the fluctuation-disordered state[33,34] or the intermediate region[35].

In analogy to the experiment, we focused on the nucleation of skyrmions from the FM state, in which the initial state holds no information about the chirality. The simulation starts at a finite but low temperature at equilibrium in the ordered FM phase. Inspired by the experimentally observed insensitivity for the switching process to details of the excitation, the laser-induced heating was modelled by the generic temperature profile shown in Fig. 5b, that is, by a sharp increase of the sample temperature $T$ followed by slower cooling (see Methods for details). To compare the simulations with the experiments, we plot the evolution of the squared Fourier transform of the local perpendicular magnetization $m_z$ in Fig. 4f. In excellent agreement with the experiment, the simulated scattering shows an initially diffuse distribution that becomes more intense and more concentrated at low $q$ as time progresses. Differences in the absolute values of the time and length scales derive from the simplifications of our model (Methods). Also note that no meaningful analogue of $I(t)$ can be extracted from our simulations because our model comprises only one layer and hence cannot reproduce the reinstatement of interlayer coupling that characterizes the experimental $I(t)$. On a short timescale (<300 ps in the experiment, <10 ps in the simulation), however, experiment and simulation exhibit qualitative agreement, which shows that the simulation is suitable to explain the microscopic mechanism of topological switching in the fluctuation state.

To understand how chirality and topology emerge, we followed the temporal evolution of the fluctuating local topological charge density $q^{\pm}$, as shown in Fig. 5b. These fluctuations are defined as $q^{\pm} = (4\pi)^{-1}\mathbf{m}\cdot(\partial_x\mathbf{m}\times\partial_y\mathbf{m})$, which we identify as fractional skyrmion

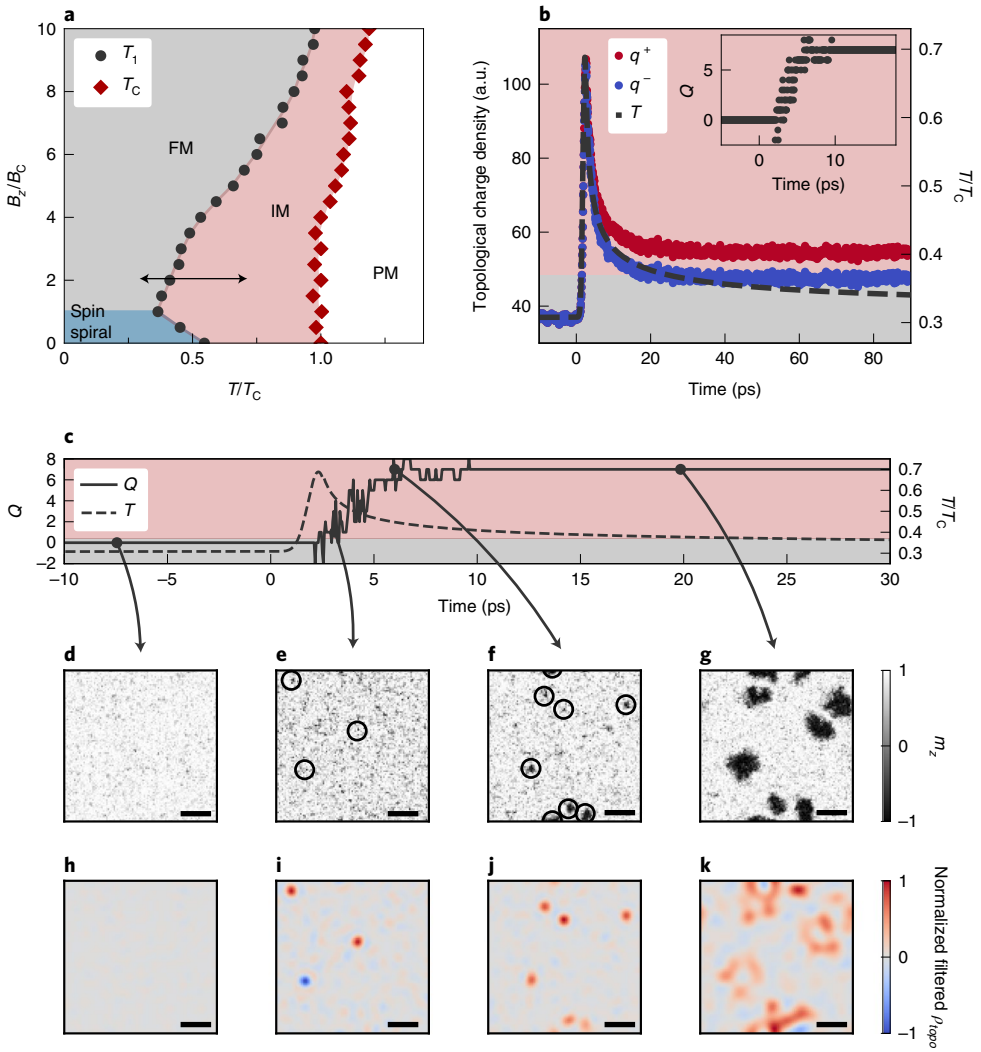


**Fig. 5 | Atomistic simulation of laser-induced skyrmion nucleation. a**, Static phase diagram of our model. $T/T_C$, reduced temperature with the Curie temperature $T_C = 29$ K; $B_z/B_c$, reduced out-of-plane magnetic field with the critical field $B_c = 0.12$ T; FM, ferromagnetic phase; IM, intermediate region; PM, paramagnetic phase. **b**, Simulated laser heating and cooling sequence (also illustrated by the double-headed arrow in **a**). The black dashed curve shows the heat-bath temperature $T$. The coloured background indicates the static FM and IM phases that would form if the temperature was varied adiabatically. The densities of skyrmion (red) and antiskyrmion (blue) fractional topological charges, as defined in the text, are plotted on the same timescale. Inset: the total integrated topological charge $Q = \int dx dy (q^+ - q^-)$ of the entire simulation area. **c**, Magnification of the evolution of $Q$ and $T$. **d**–**g**, Snapshots of the normalized out-of-plane magnetization $m_z$ at selected times, as indicated in **c**. **h**–**k**, Snapshots of the topological charge density $\rho_{topo}$ at the same times. A low-pass filter was applied to separate the agglomerated integer topological charges (skyrmions and antiskyrmions) from the high-frequency thermal fluctuations of zero-average fractional charges and normalized to the absolute maximum (see Methods for details). The thereby detected positions of skyrmions and antiskyrmions are indicated by circles in the magnetization maps. Scale bars, 20 atomic spacings. a.u., arbitrary units.

(antiskyrmion) charge densities $q^+$ ($q^-$) if the number is positive (negative)[35]. Here, $m$ is the local magnetization. The total charge $Q = \int dx dy (q^+ - q^-)$ must be integer at all times, but it does not have to be constant. Bound pairs of $q^+$ and $q^-$ with zero net topological charge were generated at all temperatures. However, shortly after the bath was heated to the intermediate region, we additionally observed topological switching, that is, a deviation of $q^+$ and $q^-$ and non-zero $Q$. This is topologically allowed in the intermediate region because enough energy is available for thermally activated switching of a cluster of a few spins[35,36], as required for skyrmion formation in our high-damping material[36].

To follow the details of the skyrmion formation process, we plot the time trace of $Q$ and $T$ in Fig. 5c, and show snapshots of the magnetization pattern and the topological charge density in Fig. 5d–k (Supplementary Video 1). $Q(t)$ exhibits rapid fluctuations on top of a steady increase while $T$ is in the intermediate region. Topological switching events can be identified by a sudden local imbalance of $q^+$ and $q^-$, that is, by a net local topological charge. This is shown in Fig. 5h–k, where we applied a dynamically adapted low-pass filter to remove all the zero-average thermal fluctuations. The initial low-pass filter cut-off of eight atomic spacings provides an estimate of the diameter of a skyrmion nuclei in our simulation. Remarkably, skyrmions and antiskyrmions did not form in pairs. Both position and time of creation of the skyrmions and antiskyrmions appeared uncorrelated. Antiskyrmions were created less frequently and their lifetime was much shorter than that of skyrmions. This explains the steady increase of total topological charge of the system. The more the system cooled down, the less frequently we observed nucleation or annihilation events. Eventually, all the switching events stopped. At this point, thermal fluctuations only changed the skyrmion shape

but not their existence. This transition occurred at ~10 ps in the simulation, which marks the end of the fluctuation state. In agreement with the experiment, only skyrmions were observed in the final state.

## Understanding of the switching dynamics

Given the combined set of experimental and theoretical results we are in a position to rationalize the mechanism and speed at which the topological charge can emerge. To begin with, our understanding is based on real-space imaging, from which we established that every texture nucleated by high-power laser pulses has the same unit topological charge.

In principle, the appearance of such a skyrmion state shares similarities with the KZM[5]. For example, based on event horizon arguments, the KZM predicts the formation of compact domains by cooling down from the laser-induced paramagnetic phase. However, the actual formation dynamics near the critical point is beyond the scope of KZM. In particular, substantial extension of the KZM is required to account for the here-observed transient fluctuation state, the non-trivial temporal evolution of the correlation length during cooling and the formation of a net global topological charge. In addition, skyrmions can form by Arrhenius activation over the topological energy barrier, as evidenced in B20 materials[11,12]. However, the topological nucleation energy barrier[25] is $8\pi At > 500 k_B T_{300K}$ for each skyrmion (where $A \approx 10\,\mathrm{pJ\,m^{-1}}$ is the exchange stiffness and $t \geq 9\,\mathrm{nm}$ is the magnetic material thickness) and the Arrhenius activation over such a large energy barrier must follow entropy-assisted heterogeneous nucleation[11,12]. Both are in contrast with our observations of a large density of skyrmions and a picosecond nucleation timescale.

Our simulations indicate the existence of a topological fluctuation state of matter, in which the topological energy barrier is effectively eliminated due to massively reduced $A$ and $t$, that is, a lack of lateral ferromagnetic order and coupling between layers. In momentum space, this state exhibits a characteristic evolution of $I(q,t)$ from a broad distribution to a well-defined peak, a feature that is experimentally confirmed. Moreover, the simulations show that in the fluctuation state a high density of topological nucleation centres is possible despite the absence of inhomogeneities in the simulation that would support such localized switching. The simulations show that this switching is enabled by the lack of long-range order in the fluctuation state, which allows highly localized dynamics of a few interacting spins, where the reduced excitation volume and the discrete nature of the spins facilitate thermally induced discontinuous topological switching, a process well beyond the continuum picture of magnonic excitations[27] (the latter are important, though, for the subsequent relaxation of the topological nucleation centres to stable skyrmions). The homogeneous nucleation mechanism observed in the simulations is consistent with the largely homogeneous nucleation probability distribution in the experiment, in accordance with the expectation that the exchange-energy-dominated nucleation in the fluctuation state should be mostly insensitive to the much weaker energy scale of local anisotropy and DMI variations that give rise to material heterogeneities responsible for pinning. Moreover, the simulations demonstrate that the total topological charge is stationary slightly before the system leaves the fluctuation state. Hence, a natural upper bound for the timescale at which a global topology emerges is given by the time the system spends in the fluctuation state. As we cannot directly infer the evolution of the topological charge in the current experiment, we define an upper bound for this timescale from the reinstatement of interlayer ferromagnetic alignment at ~300 ps. The establishment of an interlayer coherence of spin textures in our magnetostatically coupled multilayer material can be taken as an indication that the topological energy barrier has largely recovered, and we therefore conclude that topological switching is completed within this time frame. Further studies are needed to understand if and how a direct quantitative measure of the topological fluctuation state can be obtained.

Two more characteristic features of the topological fluctuation state are required for the formation of a homotopological final state. First, the topological fluctuation state supports short-range spin order, a prerequisite for the stability of a topological nucleus and a key distinction from the paramagnetic phase (even though the paramagnetic phase may be traversed before entering the fluctuation state, as indicated by the lack of an upper fluence bound). And, second, a magnetic field must break the time-reversal symmetry, which distinguishes our experiment from previous spatiotemporally resolved experiments in Pt/Co and related materials[14–16,26]. The field ensures that one polarity of skyrmion is preferred over the other and thereby leads to the creation of a net topological charge. Finally, inhomogeneous heating across the sample thickness is also expected to be of key importance for symmetric Pt/Co to break the symmetry between skyrmions and antiskyrmions. Similar to compositional gradients in ferrimagnetic materials[37], the vertical heat gradient due to the finite laser penetration depth may cause transient chiral interactions and thereby induce the required asymmetry that leads to the observed pure skyrmion final state. It will be interesting to investigate this mechanism further by studying the fluence and wavelength dependence of all-optical topological switching.

The picosecond timescale at which the global topological charge emerges is particularly surprising considering that optically induced subnanosecond switching dynamics is so far only known from ferrimagnets, in which it is facilitated by angular momentum transfer between antiparallel sublattices[27,38]. In ferromagnets, by contrast, the subnanosecond emergence of any magnetic state has only been reported for the recovery of the exact same state as that before the excitation, that is, when the dynamics is guided by the magnetic memory of a partially demagnetized material[39]. The formation of new magnetic textures was observed, for example, in CoPd after high fluence laser pulses, but was found to correlate with long remagnetization times of more than 5 ns (ref. [26]). Our results were obtained at a comparable fluence, in which full demagnetization of our sample by the laser heat is expected[15]. Still, we found that 300 ps was enough to reach 80% of the final-state magnetic scattering intensity, even though major parts of the new spin texture were oriented against the previous configuration and against the applied magnetic field. Regardless of topology, such a rapid formation of texture is unexpected and underlines that all-optical topological switching is a new form of ultrafast magnetization dynamics.

## Outlook

Using time-resolved X-ray scattering in combination with atomistic spin dynamics simulations, we demonstrated that femtosecond laser pulses can drive ferromagnetic multilayers into a high-temperature topological fluctuation state in which skyrmions are created by homogeneous nucleation at picosecond timescales. These skyrmions remain stable at room temperature. Such dynamics through a topological fluctuation state is important to understand ultrafast topological phenomena and may not be restricted to magnetic textures. Our work motivates further studies of topological switching in a large variety of systems, which ultimately may disclose the fundamental limits on the speed of topological phase transitions.

## Online content

Any methods, additional references, Nature Research reporting summaries, source data, extended data, supplementary information, acknowledgements, peer review information; details of author contributions and competing interests; and statements of data and code availability are available at https://doi.org/10.1038/s41563-020-00807-1.

Received: 30 March 2020; Accepted: 20 August 2020;
Published online: 05 October 2020

## References


1. Wall, S. et al. Ultrafast disordering of vanadium dimers in photoexcited $VO_2$. *Science* **362**, 572–576 (2018).
2. Vogelgesang, S. et al. Phase ordering of charge density waves traced by ultrafast low-energy electron diffraction. *Nat. Phys.* **14**, 184–190 (2018).
3. Zong, A. et al. Evidence for topological defects in a photoinduced phase transition. *Nat. Phys.* **15**, 27–31 (2019).
4. Stojchevska, L. et al. Ultrafast switching to a stable hidden quantum state in an electronic crystal. *Science* **344**, 177–180 (2014).
5. Zurek, W. H. Cosmological experiments in condensed matter systems. *Phys. Rep.* **276**, 177–221 (1996).
6. Kosterlitz, J. M. & Thouless, D. J. Ordering, metastability and phase transitions in two-dimensional systems. *J. Phys. C* **6**, 1181–1203 (1973).
7. Bernevig, B. A., Hughes, T. L. & Zhang, S.-C. Quantum spin Hall effect and topological phase transition in HgTe quantum wells. *Science* **314**, 1757–1761 (2006).
8. Sie, E. J. et al. An ultrafast symmetry switch in a Weyl semimetal. *Nature* **565**, 61–66 (2019).
9. Yamasaki, Y. et al. Dynamical process of skyrmion–helical magnetic transformation of the chiral-lattice magnet FeGe probed by small-angle resonant soft X-ray scattering. *Phys. Rev. B* **92**, 220421 (2015).
10. Zhao, X. et al. Direct imaging of magnetic field-driven transitions of skyrmion cluster states in FeGe nanodisks. *Proc. Natl Acad. Sci. USA* **113**, 4918–4923 (2016).
11. Wild, J. et al. Entropy-limited topological protection of skyrmions. *Sci. Adv.* **3**, e1701704 (2017).
12. Berruto, G. et al. Laser-induced skyrmion writing and erasing in an ultrafast cryo-Lorentz transmission electron microscope. *Phys. Rev. Lett.* **120**, 117201 (2018).
13. Je, S.-G. et al. Creation of magnetic skyrmion bubble lattices by ultrafast laser in ultrathin films. *Nano Lett.* **18**, 7362–7371 (2018).
14. Barman, A. et al. Ultrafast magnetization dynamics in high perpendicular anisotropy $[Co/Pt]_n$ multilayers. *J. Appl. Phys.* **101**, 09D102 (2007).
15. Pfau, B. et al. Ultrafast optical demagnetization manipulates nanoscale spin structure in domain walls. *Nat. Commun.* **3**, 1100 (2012).
16. Lambert, C.-H. et al. All-optical control of ferromagnetic thin films and nanostructures. *Science* **345**, 1337–1340 (2014).
17. Cape, J. A. & Lehman, G. W. Magnetic domain structures in thin uniaxial plates with perpendicular easy axis. *J. Appl. Phys.* **42**, 5732–5756 (1971).
18. Grundy, P. J. Magnetic bubbles and their observation in the electron microscope. *Contemp. Phys.* **18**, 47–72 (1977).
19. Büttner, F. et al. Dynamics and inertia of skyrmionic spin structures. *Nat. Phys.* **11**, 225–228 (2015).
20. Woo, S. et al. Observation of room-temperature magnetic skyrmions and their current-driven dynamics in ultrathin metallic ferromagnets. *Nat. Mater.* **15**, 501–506 (2016).
21. Montoya, S. A. et al. Tailoring magnetic energies to form dipole skyrmions and skyrmion lattices. *Phys. Rev. B* **95**, 024415 (2017).
22. Pollard, S. D. et al. Observation of stable Néel skyrmions in cobalt/palladium multilayers with Lorentz transmission electron microscopy. *Nat. Commun.* **8**, 14761 (2017).
23. Romming, N. et al. Writing and deleting single magnetic skyrmions. *Science* **341**, 636–639 (2013).
24. Büttner, F. et al. Field-free deterministic ultrafast creation of magnetic skyrmions by spin–orbit torques. *Nat. Nanotechnol.* **12**, 1040–1044 (2017).
25. Büttner, F., Lemesh, I. & Beach, G. S. D. Theory of isolated magnetic skyrmions: from fundamentals to room temperature applications. *Sci. Rep.* **8**, 4464 (2018).
26. Bergeard, N. et al. Irreversible transformation of ferromagnetic ordered stripe domains in single-shot infrared-pump/resonant-X-ray-scattering-probe experiments. *Phys. Rev. B* **91**, 054416 (2015).
27. Iacocca, E. et al. Spin–current-mediated rapid magnon localisation and coalescence after ultrafast optical pumping of ferrimagnetic alloys. *Nat. Commun.* **10**, 1756 (2019).
28. Litzius, K. et al. Skyrmion Hall effect revealed by direct time-resolved X-ray microscopy. *Nat. Phys.* **13**, 170–175 (2017).
29. Jiang, W. et al. Direct observation of the skyrmion Hall effect. *Nat. Phys.* **13**, 162–169 (2016).
30. Everschor-Sitte, K., Sitte, M., Valet, T., Abanov, A. & Sinova, J. Skyrmion production on demand by homogeneous DC currents. *New J. Phys.* **19**, 092001 (2017).
31. Eggebrecht, T. et al. Light-induced metastable magnetic texture uncovered by in situ Lorentz microscopy. *Phys. Rev. Lett.* **118**, 097203 (2017).
32. Lemesh, I. et al. Current-induced skyrmion generation through morphological thermal transitions in chiral ferromagnetic heterostructures. *Adv. Mater.* **30**, 1805461 (2018).
33. Janoschek, M. et al. Fluctuation-induced first-order phase transition in Dzyaloshinskii–Moriya helimagnets. *Phys. Rev. B* **87**, 134407 (2013).
34. Rózsa, L., Simon, E., Palotás, K., Udvardi, L. & Szunyogh, L. Complex magnetic phase diagram and skyrmion lifetime in an ultrathin film from atomistic simulations. *Phys. Rev. B* **93**, 024417 (2016).
35. Böttcher, M., Heinze, S., Egorov, S., Sinova, J. & Dupé, B. *B–T* phase diagram of Pd/Fe/Ir(111) computed with parallel tempering Monte Carlo. *New J. Phys.* **20**, 103014 (2018).
36. Koshibae, W. & Nagaosa, N. Creation of skyrmions and antiskyrmions by local heating. *Nat. Commun.* **5**, 5148 (2014).
37. Kim, D.-H. et al. Bulk Dzyaloshinskii–Moriya interaction in amorphous ferrimagnetic alloys. *Nat. Mater.* **18**, 685–690 (2019).
38. Graves, C. E. et al. Nanoscale spin reversal by non-local angular momentum transfer following ultrafast laser excitation in ferrimagnetic GdFeCo. *Nat. Mater.* **12**, 293–298 (2013).
39. Kazantseva, N., Nowak, U., Chantrell, R. W., Hohlfeld, J. & Rebei, A. Slow recovery of the magnetisation after a sub-picosecond heat pulse. *Europhys. Lett.* **81**, 27004 (2007).

## Methods

**Sample fabrication.** Multilayers of Pt/CoFeB/MgO were grown by Ar magnetron sputter deposition onto silicon nitride membranes with a seed layer of Ta(3.6 nm)/Pt(3.7 nm) and capped with Pt(2.7 nm). The Pt layers were grown at an Ar pressure of 3.5 mtorr. For all other layers, the Ar pressure was 3 mtorr. In this material stack, a sizable DMI on the order of 1.5 mJ m$^{-2}$ was previously reported[32], which led to homochiral left-handed Néel-type spin textures throughout the film thickness[40]. Pt/Co multilayers were grown on 150-nm-thick $Si_3N_4$ membranes by d.c. magnetron sputtering (radio-frequency magnetron sputtering in the case of Ta) at $2.7\times10^{-3}$ mbar Ar pressure and $6.5\times10^{-9}$ mbar base pressure. Magnetic tracks of width 10 µm were fabricated by electron-beam lithography and lift-off, followed by focused ion beam milling to reduce the track widths to the dimensions shown in the figures. The tracks were contacted with Ti(5 nm)/Au(100 nm) pads made by a two-step process of electron-beam lithography and lift-off followed by shadow-mask deposition. The holography masks on the back side of the membranes comprised a $[Cr(5\,nm)/Au(55\,nm)]_{20}$ multilayer into which the object hole and the reference holes were milled by a focused ion beam. Scanning electron micrographs of all our devices are shown in Extended Data Fig. 2.

**X-ray imaging and laser excitation.** X-ray imaging and laser excitation were performed via Fourier-transform X-ray holography in a mask-based approach[41] at beamline P04 at PETRA III in Hamburg. We used circularly polarized X-rays at the $L_3$ resonance of Co (778 eV) to obtain magnetic contrast via the X-ray magnetic circular dichroism. Magnetic contrast was obtained from helicity difference images, and sum images show transmission contrast reflecting topography in our samples (Extended Data Fig. 1). We chose to reconstruct the X-ray transmission amplitude instead of the magnetic phase contrast because amplitude images are more robust against contrast fluctuations in our set-up (in which holograms were acquired with a central beam stop). Linearly polarized laser pulses with a wavelength of 1,030 nm were generated by an Amplitude Satsuma fibre laser with software-controlled pulse duration, power, repetition rate and number of pulses. The laser was coupled into the vacuum using an upstream on-axis mirror. The laser pulse energy ($E$) and laser focus were calibrated at the position of the sample immediately after the experiment. The laser spot on the sample followed a Gaussian profile with an elliptical footprint of $\sigma_x = 40$ µm and $\sigma_y = 30$ µm (long and short axes, respectively, and s.d.). The incident laser fluence ($I$) was estimated as the peak fluence of the laser spot, $I = E/(2\pi\sigma_x\sigma_y)$. The overlap of X-ray and infrared beams was adjusted in situ using a fluorescent screen and a microscope. Stability of the laser position on the sample was confirmed by observing the same switching threshold at the beginning and at the end of a measurement series. After establishing a stable switching threshold, we used the switching threshold to calibrate the fluence and to compare measurement series of the same samples between different beamtimes. The error in fluence due to these beam position uncertainties was estimated to be 10%.

The process of reconstructing magnetic images via X-ray holography is illustrated in Extended Data Fig. 1. We first recorded holograms with positive and negative helicity light. The set-up to record holograms is discussed in detail in the literature[41,42]. By subtracting the two helicity holograms from each other we isolated the magnetic contribution. An inverse Fourier transform yielded a Patterson map, which included the cross-correlations between the specimen transmission function and the delta-like reference transmission functions. These cross-correlations are the reconstructions of the magnetic images, convolved with the reference beam profile. Finally, we propagated the reconstruction to the position along the beam axis where the reference is smallest, and hence provided the sharpest image[43]. The final result is the image shown in Extended Data Fig. 1f. All images in the main text were reconstructed in this way.

**LTEM.** LTEM was performed at the Göttingen Ultrafast Transmission Electron Microscope, a modified JEOL 2100F that allows for in situ optical sample excitation[31,44]. The microscope was operated at 200 kV and in a low magnification mode, in which the main objective lens was normally current free and could be used to apply an arbitrary out-of-plane magnetic field at the sample, which ranged from zero to several hundred millitorrs. Images where acquired using a CEOS Energy-Filtering and Imaging Device (CEFID)—filtering out inelastically scattered electrons with an energy loss larger than 6 eV—and a TVIPS XF416. Magnetic contrast was obtained in overfocus imaging conditions[45].

The skyrmion state was prepared by initially saturating the sample in an out-of-plane magnetic field of 250 mT and then reducing the field to 25 mT and exciting the sample with an optical burst of laser pulses at a wavelength of 770 nm. The burst consisted of 20 pulses each with a fluence of 8 mJ cm$^{-2}$ at a 610 kHz repetition rate and was used to compensate for the smaller maximum achievable fluence of the set-up.

**Atomistic simulations.** Atomistic simulations were carried out on a square lattice in a volume of $100\times100\times1$ atomic spacings (unit cells). Periodic boundary conditions were employed in the $x$ and $y$ directions. We considered the Heisenberg Hamiltonian:

$$H = -\sum_{ij} J_{ij}(\mathbf{m}_i \cdot \mathbf{m}_j) - \sum_{ij} \mathbf{D}_{ij} \cdot (\mathbf{m}_i \times \mathbf{m}_j) - \sum_i K m_{i,z}^2 - \sum_i \mu_0 M_s (m_{i,z} B_z) \quad (1)$$

Here, $i$, $j$ enumerate lattice sites and $\mathbf{m}_i = \mathbf{M}_i/M_s$ are unit vectors along the local spin direction and $m_{i,z}$ is the out-of-plane component. The model parameters are the atomic spin moment $M_s = 4.66\,\mu_B$, first nearest-neighbour exchange interaction $J_1 = 1.5$ meV (zero otherwise) and easy axis anisotropy $K = 0.46$ meV along the out-of-plane direction. The DMI vectors $\mathbf{D}_{ij}$ are in-plane and perpendicular to the spin pair position vector $\mathbf{r}_{ij}$, which favours Néel-type spin textures. The magnitude of $\mathbf{D}_{ij}$ is $D_1 = 0.6$ meV for nearest neighbours and zero otherwise. $B_z$ is the variable external out-of-plane magnetic field. Note that in our experimental multilayer material, non-collinear textures, such as stripe domains and skyrmions, were stabilized primarily by non-local stray field interactions[25]. To compensate for the fact that our model, due to its computational complexity, does not include stray field interactions, we increased the values of $D/J$ and $D/K$ compared with typical values of monolayer-thick films[35] to a value at which the $B = 0$, $T = 0$ state resembles the experimentally observed stripe domain state (see Lemesh et al.[32] for details).

Magnetization dynamics simulations follow the Landau–Lifschitz–Gilbert equation:

$$\frac{d\mathbf{m}_i}{dt} = -\gamma \mathbf{m}_i \times \mathbf{B}_i + \alpha \mathbf{m}_i \times \frac{d\mathbf{m}_i}{dt} - \gamma \mathbf{m}_i \times \boldsymbol{\zeta}(t) \quad (2)$$

where $\mathbf{B}_i$ is the effective magnetic field at spin $i$, $\gamma = 1.76\times10^{11}$ A s kg$^{-1}$ is the gyromagnetic ratio and $\alpha = 0.3$ is the Gilbert damping. This equation was numerically solved in time steps of 1 fs using a Heun solver (and cross-checked with a Euler solver, which both gave the same result). At each time step, the internal field was determined from the Hamiltonian equation (1) as:

$$\mathbf{B}_i = -\frac{1}{M_s}\frac{\partial H}{\partial \mathbf{m}_i} \quad (3)$$

The dynamics simulations were performed in an external field of $B_z = 2.05\,B_c$, where $B_c = 0.12$ T defines the transition from a spin spiral to the ferromagnetic phase at low temperature. The stochastic field $\boldsymbol{\zeta}(t)$ describes the coupling of the magnetic system to the finite temperature fluctuations of the non-magnetic degrees of freedom of the sample. At each time, all the Cartesian components $\nu$ of this field were randomly generated according to a Gaussian probability distribution with zero mean:

$$\langle \zeta^\nu(t) \rangle = 0 \quad (4)$$

By the fluctuation–dissipation theorem, the spatial (lattice sites $i$, $j$) and temporal correlations between the different components $\nu$, $\kappa$ of the stochastic field is determined by the sample temperature $T$ and the dimensionless damping parameter $\alpha$ via:

$$\left\langle \zeta_i^\nu(t)\zeta_j^\kappa(t') \right\rangle = 2\alpha \frac{k_B T}{\gamma M_s} \delta_{i,j}\delta_{\nu,\kappa}\delta(t-t') \quad (5)$$

We used the following function to model the temporal evolution of the sample temperature:

$$T(t) = \begin{cases} T_0 & \text{if } t < t_0 \\ T_0 + I_0 \exp\left(-\frac{(t-t_0-t_M)^2}{\sigma^2}\right) & \text{if } t_0 < t < t_1 \\ T_0 + \frac{I_1}{(t-t_0-t_m)^k} & \text{if } t_1 < t \end{cases} \quad (6)$$

where $t_0 = 0$ ps defines the beginning of the laser pulse, $t_1 = 2.6$ ps, $t_M$ corresponds to the maximum peak of intensity $I_0$ and mean height width $\sigma$. The cooling down is modelled by an inverse polynomial of power $k$ and of intensity $I_1$, shifted by the parameter $t_m$. The data presented in Fig. 5 of the main paper correspond to $I_0 = 0.309\,T_C$, $I_1 = 0.209\,T_C$, $t_M = 2.2$ ps, $t_m = 1.7$ ps, $\sigma = 0.7$ ps and $k = 0.54$, a temperature profile inspired by typical excitation curves of the electron temperature system by a femtosecond laser pulse[46]. The generic choice was motivated by the experimentally observed robustness of the nucleation process to the laser fluence, that is, to the amplitude and shape of the applied heat pulse. The temperature $T_0$ was chosen to start the simulation in the FM phase, $T_0 = 0.307\,T_C$. All the temperatures are given in units of the Curie temperature, which is $T_C^{exp} = 650$ K in Pt/CoFeB/MgO (ref. [32]) and $T_C = 29$ K in the simulation. This low simulation value has no absolute meaning other than to help us reduce the computation time. For similar reasons, we used a faster cooling time than in the experiments, which leads to the discrepancies in absolute timescales.

Monte Carlo simulations were carried out to obtain the phase diagram presented in Fig. 5a. Parallel tempering Monte Carlo was employed to overcome possible local minima created by metastable states, such as isolated skyrmions and antiskyrmions. We simulated 180 different replicas with temperatures that were uniformly distributed between 1 and 60 K ($T_C = 29$ K). The different replicas were swapped 2,000 times and $10^6$ autocorrelation steps were used between each swap.

The starting configuration was chosen as the ferromagnetic or the spin spiral ground state at $T = 0$ K, depending on the magnetic field $B_z$.

**Low-pass filtering of the topological charge density.** To apply the low-pass filter, we multiplied the simulated charge density distributions in reciprocal space with a circular binary mask. The mask was convolved with a Gaussian (s.d. of two reciprocal unit cells) to reduce ringing artefacts in the real-space maps. We used the fast Fourier transform algorithm to numerically transform the two-dimensional real-space charge densities to reciprocal space and back. For a mask radius of $r$ (in reciprocal unit cells), this effectively averaged out all fluctuations with a real-space periodicity smaller than $1/r$. For the data shown in Fig. 5h–j, a single reciprocal unit cell has a size of 1/(100 atomic spacings). Thus, the utilized mask radius of 12 reciprocal unit cells removed fluctuations with real-space periodicities shorter than $100/12 \approx 8$ atomic spacings. The specific value of 12 reciprocal unit cells was chosen as the value that best highlighted the position of the skyrmions and antiskyrmions during the fluctuation state (Fig. 5i,j). Note that we know the total number of skyrmions minus the total number of antiskyrmions from the integrated topological charge (Fig. 5c). The optimum filter radius changed towards later times and is adjusted to four reciprocal unit cells in Fig. 5k. For display in Fig. 5, the filtered data were first normalized to the same total topological charge as before filtering and then rescaled by a factor $1/\pi r^2$ to account for the low-pass filter blurring.

**Time-resolved SAXS.** SAXS measurements of the all-optical topological switching were conducted at beamline SCS at the European XFEL. The $[Pt/Co]_{15}$ magnetic materials (see Sample fabrication above) were grown on stoichiometric (high-stress) $Si_3N_4$ membranes because these membranes remain flat even after material deposition, as confirmed by optical inspection. Therefore, the only remaining source of scattering was the magnetic texture of the sample. The membrane size was 200 µm × 200 µm, much larger than the X-ray spot (30 µm in diameter, full-width at half-maximum). The infrared laser beam (wavelength 1,030 nm) was focused to a spot size of $\sigma_x = 142$ µm and $\sigma_y = 120$ µm (Gaussian s.d. along $x$ and $y$, respectively), which lead to a homogeneous fluence of ~50 mJ cm$^{-2}$ within the X-ray spot size (estimated by measuring the laser power before the vacuum incoupling mirror). The spatial overlap of the infrared laser and the X-ray beam was measured by a camera image of both beams on an X-ray fluorescent pyrolytic boron nitride screen at the sample position, which exhibited visible light fluorescence on X-ray illumination and also diffusely reflected the infrared beam. The temporal overlap (time zero) was adjusted in two steps. Coarse time zero was determined by measuring the photocurrent of the free-electron laser and optical pulses at the conductive tip of a coaxial cable. The fine temporal overlap was measured using the specular reflectivity of the infrared beam at a $Si_3N_4$ surface, which transiently decreases when the $Si_3N_4$ crystal is exposed with X-rays[47].

The X-ray beam was monochromatized to the photon energy of maximum Co absorption at 778.9 eV (~240 meV bandwidth) using the second order of the monochromator to suppress higher harmonics. The beam was circularly polarized by transmission through a perpendicular magnetic TbCo film, even though the polarization has no relevance for the results presented here. The intensity of every X-ray pulse after the monochromator was measured using a gas absorption monitor and the result was used to normalize all the detected scattering patterns. These scattering patterns were recorded by a DEPFET sensor with signal compression (DSSC) detector[48,49] 1.44 m downstream of the sample. The detector had 1,024 × 1,024 pixels, arranged in 16 ladders of 128 × 512 hexagonal pixels with Cartesian spacings of 236 and 204 µm in the $x$ and $y$ directions, respectively[50]. We applied a mask to remove parasitic infrared light and defective pixels from the recorded data, as discussed in detail in Supplementary Section 6. The detector position was chosen such that the intense transmitted and forward-scattered X-ray beam at and close to $q = 0$ was centred on a gap between the detector ladders. All the data were recorded by first saturating the sample at 263 mT and subsequently reducing the field to 83 mT, at which a train of three X-ray pulses and one infrared laser pulse was applied (Fig. 1b). Before and after each transient and final-state X-ray pulse, we recorded additional dark frames, that is, six camera frames in total per train. Owing to communication issues with the magnet power supply, not all the X-ray pulse trains were acquired in this sequence. We applied several filters to select the correct trains with statistically meaningful information, as described in detail in Supplementary Section 7. Moreover, we determined the threshold for X-ray-induced skyrmion nucleation and attenuated the incoming beam to well below that threshold (Supplementary Section 5 and Extended Data Fig. 6). The data acquisition and analysis were performed using the Karabo infrastructure of the European XFEL[51].

All the data were corrected by subtracting dark frames, that is, data recorded after the experiment without X-ray or infrared light. Furthermore, we subtracted the average of the dark frames before and after the transient and final state from the respective state. All the scattering patterns were normalized to the incident X-ray intensity. In addition, the scattering patterns in Fig. 4a–c were normalized to the maximum counts in the final state image (Fig. 4c). $I(t)$ in Fig. 4d was obtained by integration between $q_{min} = 0.021$ nm$^{-1}$ and $q_{max} \approx 0.155$ nm$^{-1}$. The same ranges were applied to transient and final state integrals. The lower integration limit was given by the central gap and the upper limit was introduced because higher $q$ data were found to contribute many pixels with a high noise level and were therefore excluded from this plot. The time-dependent intensity was fitted with a logistic function $I(t) = L/(1 + \exp(-(t - t_0)/\tau_{eq}))$ to extract the equilibration time constant $\tau_{eq}$, the inflection time $t_0$ and the amplitude $L$. To estimate the error of the fit parameters, $q_{max}$ was varied between 0.08 and 0.255 nm$^{-1}$ and the s.d. of the resulting arrays of normalized intensities and logistic fit values are reported as error bars (Supplementary Section 9). Note that this is justified because the particular choice of $q_{max}$ determines the magnitude of the total intensity in Fig. 4d, but not the functional shape, and the equilibration time constant and saturation beyond 300 ps are robustly obtained for $q_{max}$ in the given range.

The data in Fig. 4e were obtained by averaging the intensity in rings of constant momentum transfer around the centre (that is, by integrating the intensity and dividing by the number of contributing pixels). Figure 4f shows the similarly averaged squared Fourier transform of the $m_z(x,y,t)$ maps shown in Fig. 5d–g, which represents the anticipated X-ray scattering patterns of the simulation. The experimental data have a lower noise compared with the simulations because the area probed by the X-ray pulse greatly exceeds the simulation area. To correct for a slow drift of the dark counts of the camera, we subtracted the initial state in Fig. 4d,e before normalizing to the average peak intensity of the final state scattering (Supplementary Section 8).

The correlation length and estimate for the skyrmion diameter were determined from the peak position $q_{peak}$ in the $I(q)$ spectra and a Guinier fit of the high-$q$ shoulder of the peak[52]. The Guinier fit parameter is proportional to the mean diameter of the scattering particles. The proportionality factor depends on the shape and density of the particles. We estimated this factor using the known average size of skyrmions in the final state, as determined from Fig. 2 (see the size histogram in Supplementary Fig. 11). The remaining error of the final state fits is hence only an error of the linear regression. The error of the skyrmion diameter in the transient state was estimated as 30% of the diameter value, based on the $q$ range to which we have applied the Guinier fit[52]. The correlation length was determined based on a local parabolic fit of $q_{peak}$ (a more complex fitting with a Voigt function was found to yield the same results). The error bars of the correlation length in Fig. 4d represent the fit error of $q_{peak}$. The procedure and fit results are discussed in detail in Supplementary Section 10.

## Data availability

The data represented in Fig. 2 are provided in Extended Data Figs. 2–4. The data represented in Figs. 3–5 are available at https://doi.org/10.5281/zenodo.4017322. Raw data generated at the European XFEL large-scale facility are available at https://doi.org/10.22003/XFEL.EU-DATA-002252-00.

## Code availability

The data analysis code used in this study is available with identifiers https://doi.org/10.5281/zenodo.4017322. The code for the atomistic simulations is available from the corresponding author upon reasonable request.

## References


40. Litzius, K. et al. The role of temperature and drive current in skyrmion dynamics. *Nat. Electron.* **3**, 30–36 (2020).
41. Eisebitt, S. et al. Lensless imaging of magnetic nanostructures by X-ray spectro-holography. *Nature* **432**, 885–888 (2004).
42. Büttner, F. in *Holographic Materials and Optical Systems* (eds Naydenova, I., Babeva, T. & Nazarova, D.) (InTech, 2017).
43. Geilhufe, J. et al. Achieving diffraction-limited resolution in soft-X-ray Fourier-transform holography. *Ultramicroscopy* **214**, 113005 (2020).
44. Feist, A. et al. Ultrafast transmission electron microscopy using a laser-driven field emitter: femtosecond resolution with a high coherence electron beam. *Ultramicroscopy* **176**, 63–73 (2017).
45. Schneider, M., Hoffmann, H. & Zweck, J. Lorentz microscopy of circular ferromagnetic permalloy nanodisks. *Appl. Phys. Lett.* **77**, 2909–2911 (2000).
46. Koopmans, B. et al. Explaining the paradoxical diversity of ultrafast laser-induced demagnetization. *Nat. Mater.* **9**, 259–265 (2010).
47. Krupin, O. et al. Temporal cross-correlation of X-ray free electron and optical lasers using soft X-ray pulse induced transient reflectivity. *Opt. Express* **20**, 11396–11406 (2012).
48. Porro, M. et al. Development of the DEPFET sensor with signal compression: a large format X-ray imager with mega-frame readout capability for the European XFEL. *IEEE Trans. Nucl. Sci.* **59**, 3339–3351 (2012).
49. Hansen, K. et al. Qualification and integration aspects of the DSSC mega-pixel X-ray imager. *IEEE Trans. Nucl. Sci.* **66**, 1966–1975 (2019).
50. Erdinger, F. et al. The DSSC pixel readout ASIC with amplitude digitization and local storage for DEPFET sensor matrices at the European XFEL. In *2012 IEEE Nuclear Science Symposium and Medical Imaging Conference Record (NSS/MIC)* 591–596 (2012).
51. Fangohr, H. et al. Data analysis support in Karabo at European XFEL. In *TUCPA01, International Conference on Accelerator and Large Experimental Control Systems* 245–252 (JACOW, 2018).

52. Feigin, L. A. & Svergun, D. I. *Structure Analysis by Small-Angle X-Ray and Neutron Scattering* (ed. Taylor, G. W.) (Plenum, 1987).

## Acknowledgements

M.B. and B.D. gratefully acknowledge computing time at the Mogon supercomputers. We acknowledge the European XFEL in Schenefeld for provision of XFEL beamtime at the SCS instrument and thank the instrument group and facility staff for their assistance. In particular, we thank M. Teichmann, J. T. Delitz, A. Reich, C. Broers, M. Bergemann, E. Kamil, T. Kluyver, H. Fanghor, J. Moore, J. Engelke, M. Kuster, S. Hauf, K. Hansen, P. Fischer, C. Fiorini, D. Boukhelef, J. Szuba and K. Wrona for providing the instrumentation and infrastructure that enabled our experiment at the European XFEL. We thank M. Wieland and M. Drescher, Universität Hamburg, for providing us with their mobile laser hutch for the experiments at DESY. Work at MIT was supported by the DARPA TEE programme. Devices were fabricated using equipment in the MIT Microsystems Technology Laboratory and the MIT Nanostructures Laboratory. The samples were further manufactured at the TU Berlin Nano-Werkbank, which was supported by EFRE under contract no. 20072013 2/22. B.P., L.-M.K., K.G. and S.E. acknowledge financial support from the Leibniz Association via grant no. K162/2018 (OptiSPIN). L.C. acknowledges financial support from the NSF Graduate Research Fellowship Program and from the GEM Consortium. M.B. and B.D. acknowledge financial support from the Alexander von Humboldt Foundation, the Graduate School Materials Science in Mainz and the Transregional Collaborative Research Center (SFB/TRR) 173 SPIN+X. T.R.H. acknowledges the support of a postdoctoral fellowship from the Alexander von Humboldt Foundation. J.H.M. acknowledges funding from the Nederlandse Organisatie voor Wetenschappelijk Onderzoek (NWO) by a VENI grant and the Shell-NWO/FOM initiative 'Computational sciences for energy research' of Shell and Chemical Sciences, Earth and Life Sciences, Physical Sciences, FOM and STW.

## Author contributions

B.P., F.B., G.S.D.B. and S.E. conceived the study. F.B., C.M.G., M.S., D.E., A. Churikova, I.L. and M.H. fabricated the samples. B.P., F.B., M.S., C.M.G., P.H., C.K., A.W., K.G., L.-M.K., C.S., C.v.K.S., J.F., A.C., S.H., L.C., S.Z. and K.B. performed the experiments at DESY and F.B., B.P., M.S., G.M., C.K., K.G., L.-M.K., S.H., L.C., D.S., R.C., L.M., J. Schlappa, A.Y., L.L.G., N.G., A. Scherz, C.D., R.G., D.H., J.Z., M.T. and D.L. performed the experiments at XFEL. F.E., A. Castoldi, S.M., M.P. and A. Samartsev remotely supported the DSSC detector calibration and operation. J.H.G., M.M. and T.R.H. performed the LTEM experiments. F.B., B.P., M.S., K.G., P.H., C.K. and A.W. analysed the X-ray experiments. B.D. and M.B. performed the atomistic modelling with support from J.H.M. F.B., B.P., J.H.M. and B.D. interpreted the results. B.P., F.B., M.S., A.W., K.G. and B.D. prepared the figures and F.B. and J.H.M. wrote the manuscript with input from B.P., B.D., G.S.D.B. and S.E. Supervision was by C.R., J. Sinova, G.S.D.B. and S.E. All the authors commented on the manuscript.

## Competing interests

The authors declare no competing interests.

## Additional information

**Extended data** is available for this paper at https://doi.org/10.1038/s41563-020-00807-1.

**Supplementary information** is available for this paper at https://doi.org/10.1038/s41563-020-00807-1.

**Correspondence and requests for materials** should be addressed to F.B. or B.P.

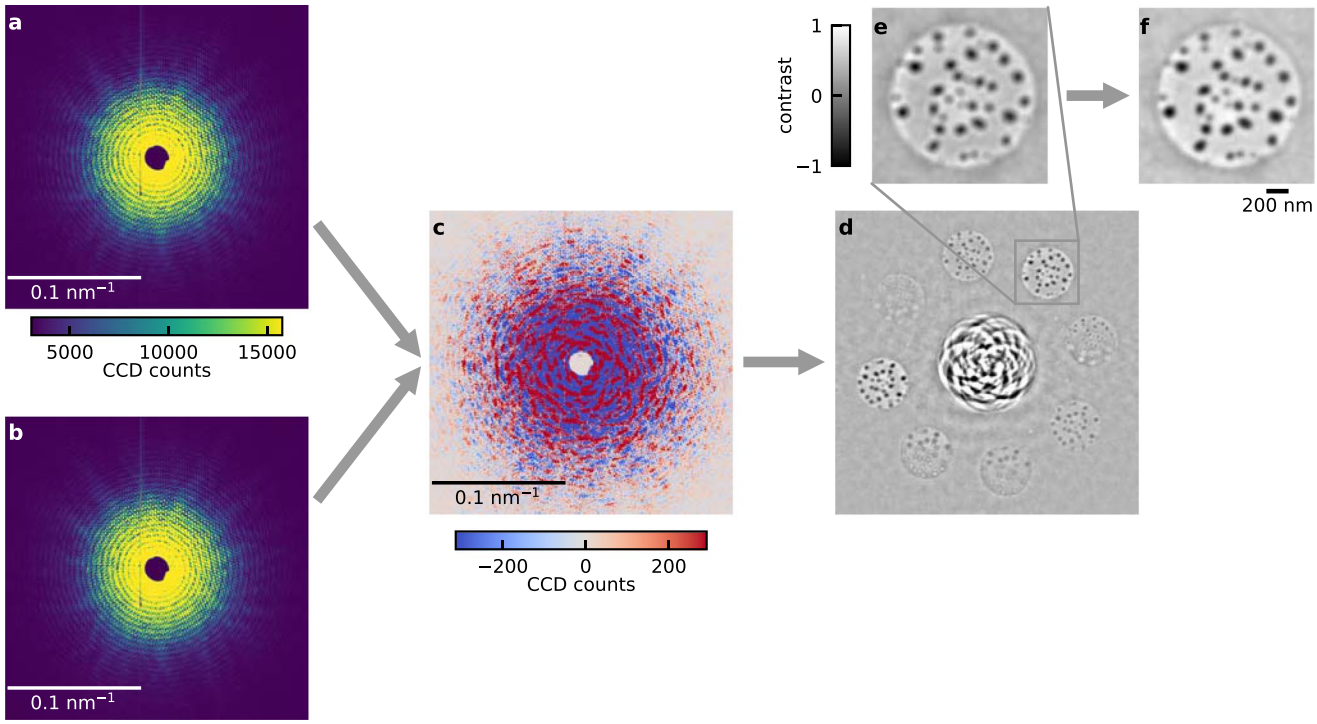


**Extended Data Fig. 1 | Process of holographic image reconstruction. a**, Hologram recorded with positive helicity light. **b**, Hologram recorded with negative helicity light. **c**, Difference hologram (positive minus negative helicity hologram). **d**, Patterson map (Fourier transform of difference hologram) showing four reconstructions and their complex conjugates. **e**, Magnification of a selected reconstruction. **f**, Reconstruction propagated to the reference focus point[43].

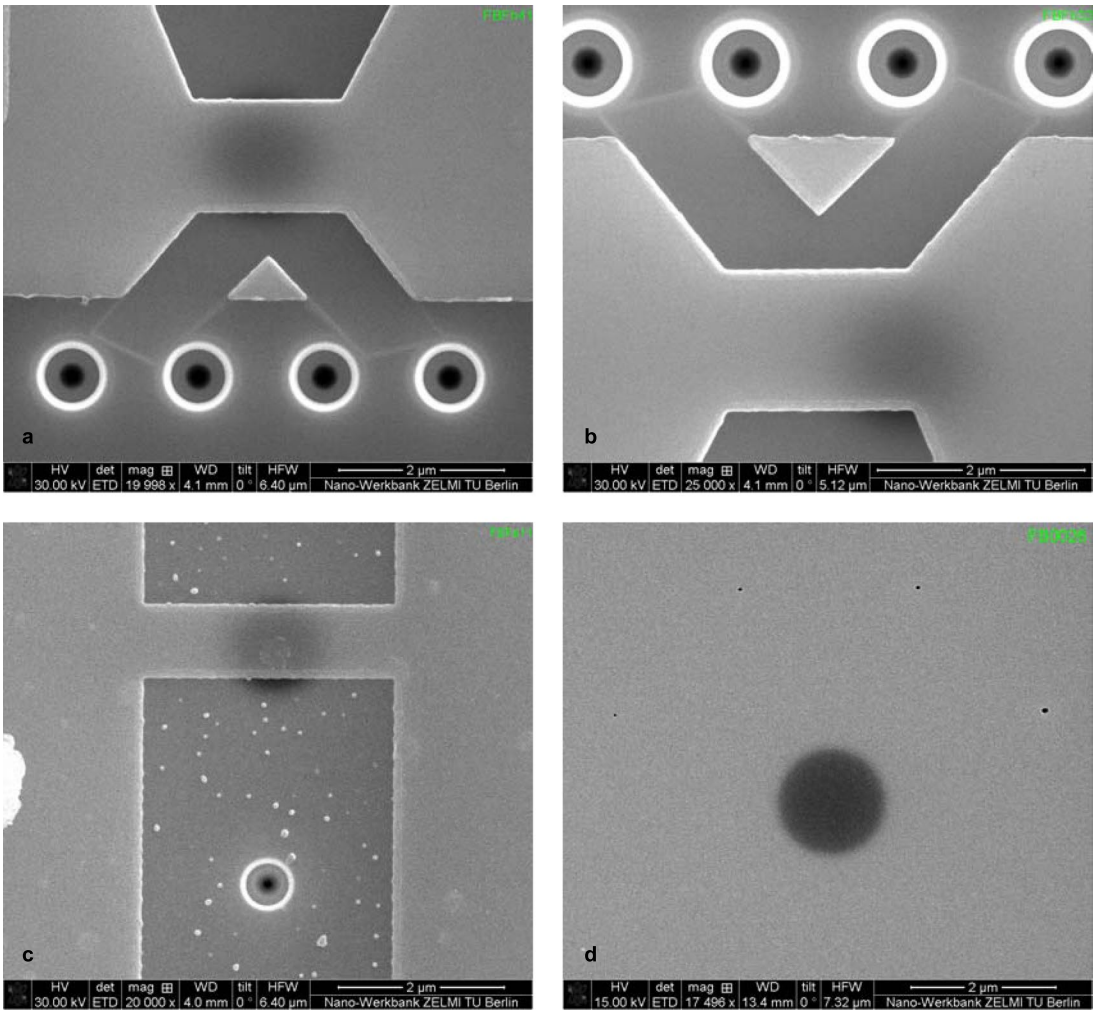


**Extended Data Fig. 2 | Scanning electron micrographs of the holography samples employed in this study. a**–**c**, Pt/CoFeB/MgO samples with patterned tracks for current injection. The holographic field of view (FOV) is defined by an aperture in the Cr/Au mask on the opposite sample side and is visible as shadow behind the tracks. The reference pinholes (four pinholes in (a) and (b), one pinhole in (c)) have their smallest exit aperture also at the opposite sample side, that is, the mask side. The sample in (a) was used for Figs. 2a and 3, sample in (b) for Fig. 2b, and the sample in (c) for Supplementary Section 1. **d**, Pt/Co sample with continuous magnetic film. The FOV appears as a shadow approximately in the center of the image and is surrounded by four reference pinholes with their smallest exit on the Pt/Co film side. The sample was used for Fig. 2c.

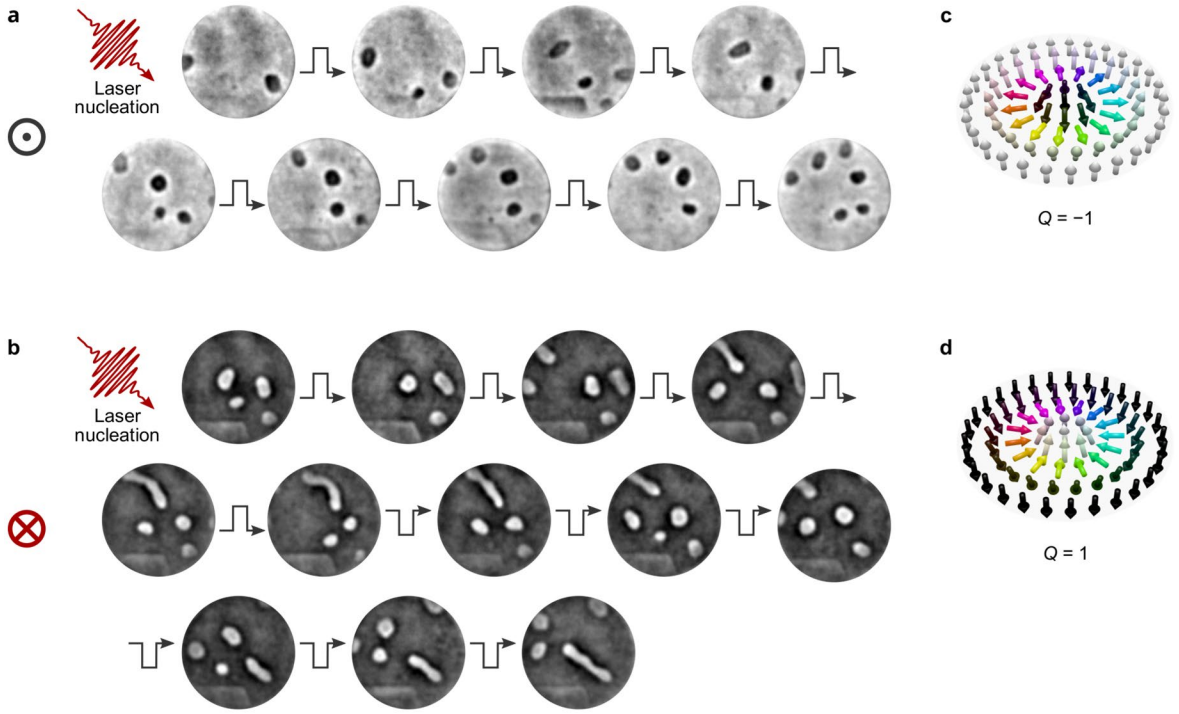


**Extended Data Fig. 3 | Measurement of the skyrmion topology via the skyrmion Hall effect. a**, For $B_z = 37$ mT. **b**, For $B_z = -36$ mT. The first image in each sequence was produced by a single >16 mJ/cm$^2$ laser pulse from a saturated state. Between subsequent images, single current pulses of the indicated polarity and direction (4 ns duration and between $7 \times 10^{11}$ A/m$^2$ and $9 \times 10^{11}$ A/m$^2$ in amplitude) were applied. The size of all circles is 1.3 μm. **c**,**d**, Spin structures of a negative polarity (black in x-ray images) and positive polarity (white) skyrmion, respectively.

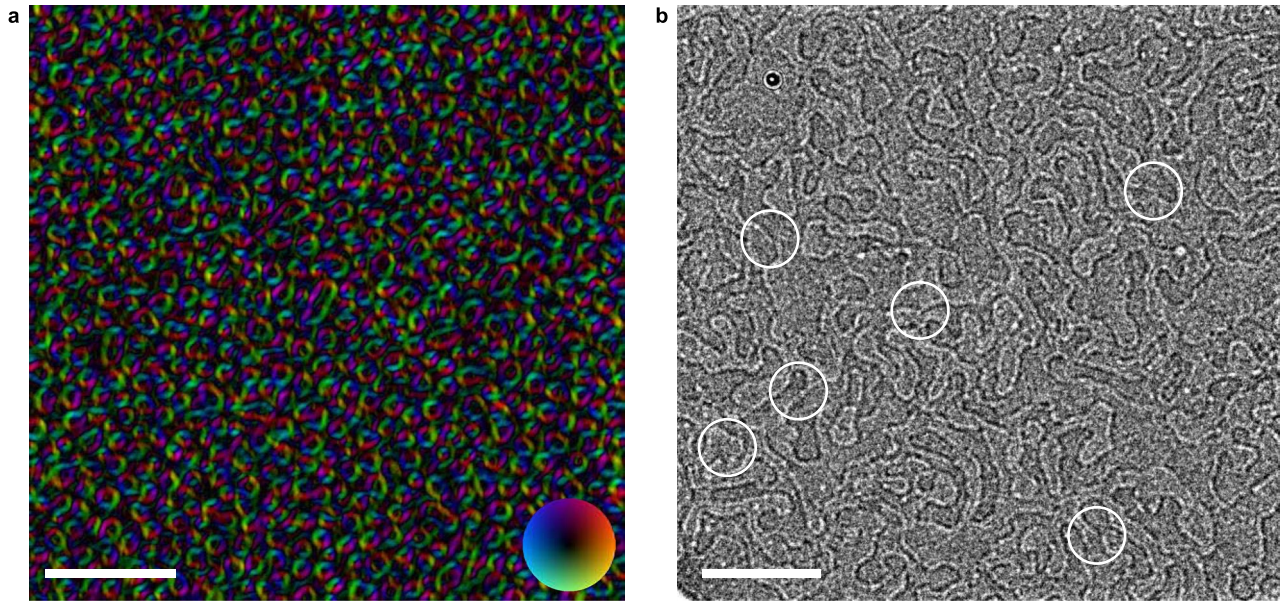


**Extended Data Fig. 4 | Lorentz transmission electron (L-TEM) micrographs of Pt/Co. a**, Transport of intensity reconstruction Fig. 2d of the main paper. The color shows in-plane orientation of magnetization, as indicated by the color wheel. **b**, Representative L-TEM image of a stripe domain state at zero field obtained by adiabatic field cycling. White circles highlight vertical Bloch lines (note that the signal-to-noise ratio is not sufficient in this case to perform the TIE analysis). Both images were recorded in overfocus conditions[45]. Scale bars, 1 μm.

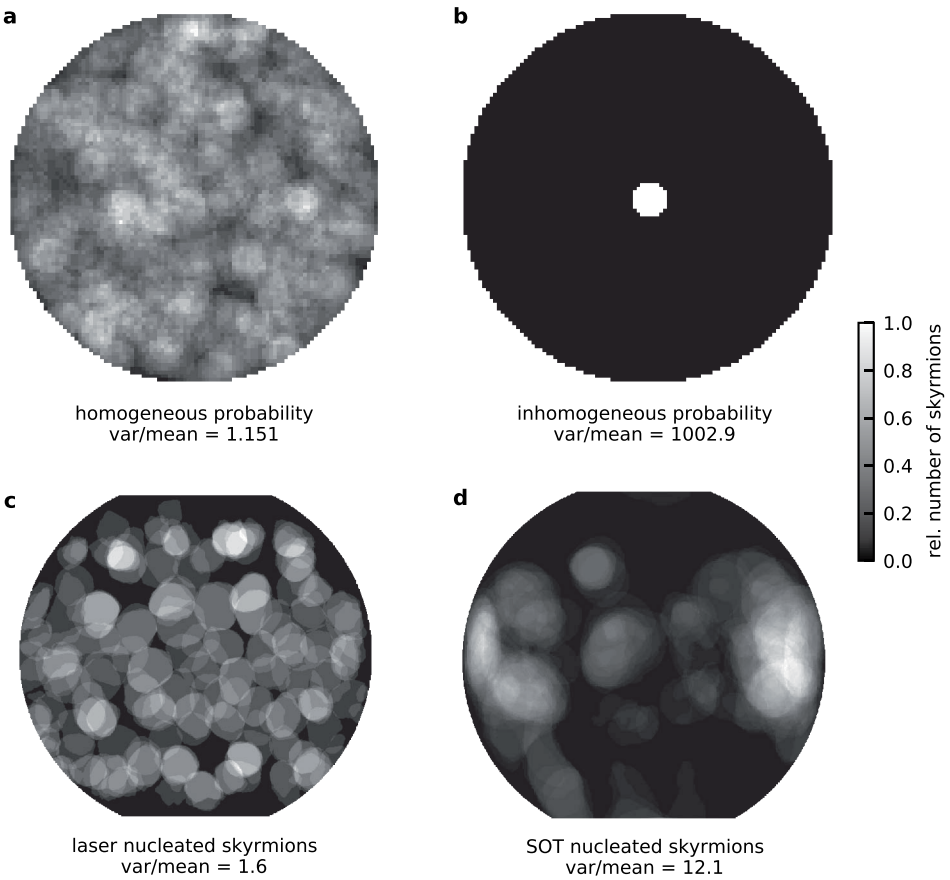


**Extended Data Fig. 5 | Simulated and experimentally observed spatial distribution of nucleated skyrmions. a**, Simulated integrated skyrmion count of 1000 skyrmions (10 px diameter) distributed according to a homogeneous nucleation probability in a 100 px diameter field of view. **b**, 1000 skyrmions distributed with 100 % probability in the central pixel. **c**, Experimentally observed distribution of optically-nucleated skyrmions (reproduced from Fig. 3 in the main text). **d**, Experimentally observed distribution of spin–orbit torque nucleated skyrmions (reproduced from[24]). The horizontal diameters of the fields of view are 100 px in (a) and (b), 1490 nm in (c) and 900 nm in (d). See Supplementary Section 4 for details.

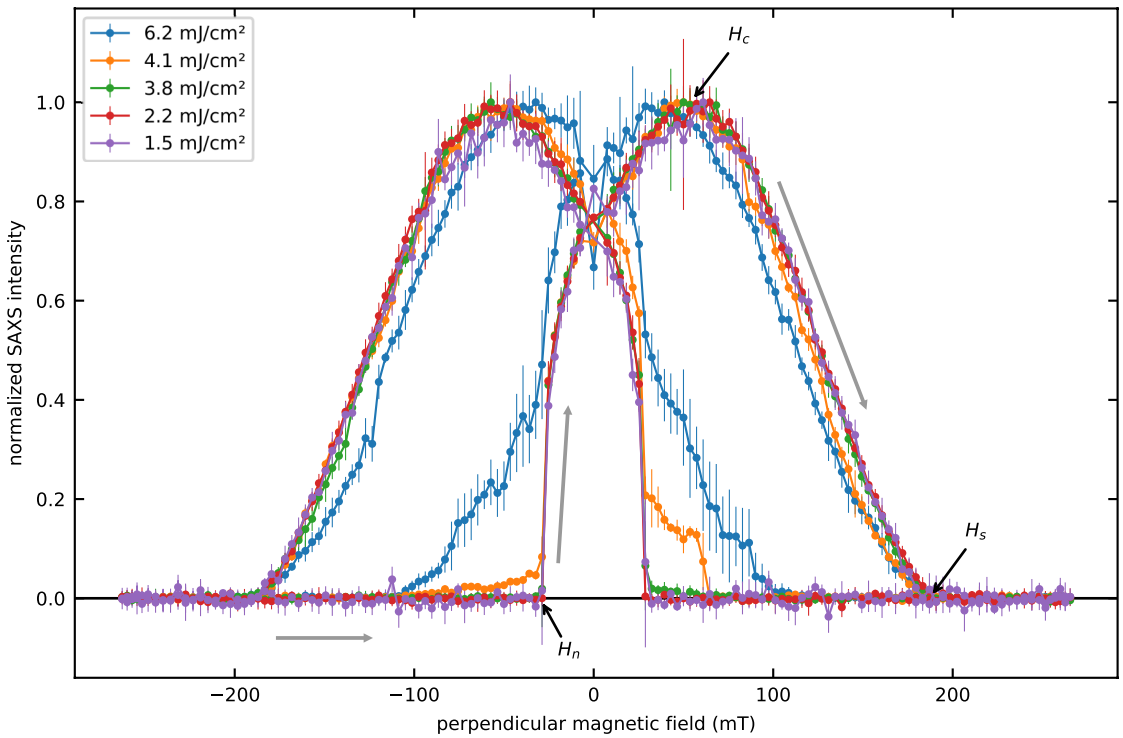


**Extended Data Fig. 6 | Small-angle x-ray scattering during a magnetic field sweep recorded with various attenuation levels of the x-ray beam.** The membrane sample is topographically homogeneous, which means that any scattering is due to non-uniformities in the magnetic landscape. Arrows indicate the saturation field $H_s$ (the field at which the scattering signal becomes zero), the nucleation field $H_n$ (the field at which the scattering signal starts to deviate from the background value) and the coercive field $H_c$ (the field at which the average magnetization is zero). Light gray arrows indicate the field sweep direction. Spectra were recorded for variable x-ray fluence by varying the transmission in a gas attenuator. The legend states the maximum peak fluence values encountered, assuming a Gaussian beam profile with a width of 30 μm (FWHM). X-ray induced skyrmion nucleation and annihilation is evidenced by an increased domain nucleation field and a reduced saturation field, respectively.

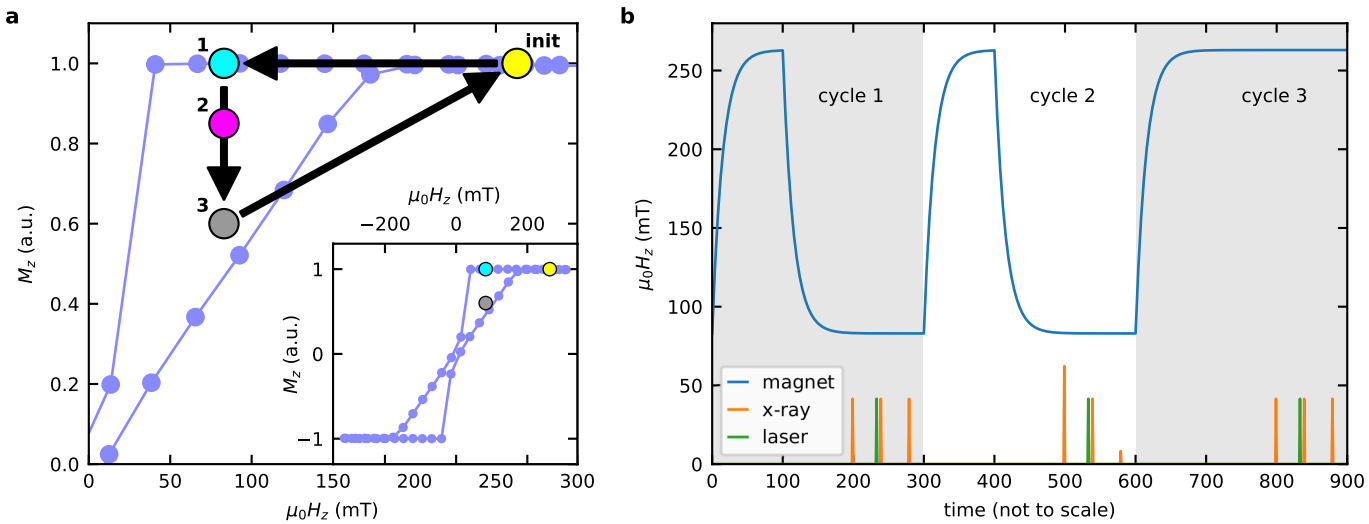


**Extended Data Fig. 7 | Schematic of the experimental sequence. a**, Hysteresis loop of Pt/Co and illustration of the measurement cycle and static hysteresis loop of the magnetic multilayer. The measurements starts at 'init' by saturating the sample (263 mT) and reducing the field to the open hysteresis area (83 mT, point 1). The laser pulse then nucleates skyrmions (3) via a transient state (2). The inset shows the full hysteresis loop of our Pt/Co multilayer. **b**, Schematic of the time traces of magnetic field, x-ray pulses, and infrared laser pulses during three successive cycles. Ideally each cycle would start with a field sweep to saturate the same and then keep the sample at remanence at $\mu_0 H_z = 83$ mT. The pump–probe sequence consisting of three x-ray pulses and one infrared laser pulse would be applied during this stable low field time. The second and third cycle illustrate possible deviations from this scheme. As shown in the second cycle, the intensity of x-ray pulses can vary wildly and in some cases one of the three x-ray pulse intensities is so low that no conclusion can be drawn from the data. Moreover, as illustrated in the third sequence, the magnetic field did not always respond to the set commands, in which case no skyrmions were nucleated. Both the second and the third type of trains were rejected from the analysis.

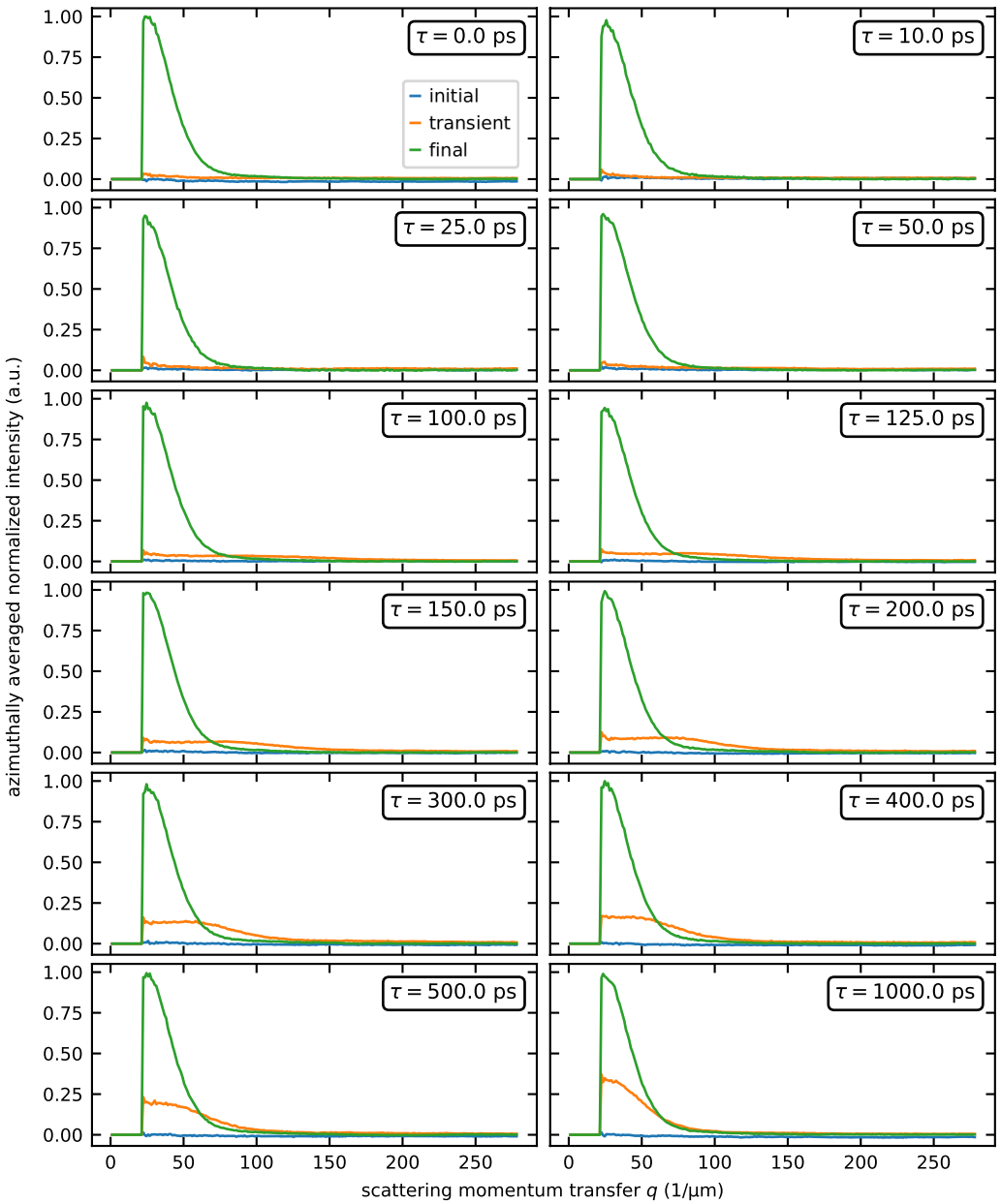


**Extended Data Fig. 8 | Scattering spectra at all measured time delays.** Orange curves show the azimuthally averaged time-dependent scattering data, which is almost constant as a function of $q$ for small delays and localizes towards smaller $q$ at later times. Blue and green lines show the corresponding initial and final state spectra, respectively. The low $q$ cutoff is due to missing pixels of the detector around the central beam.

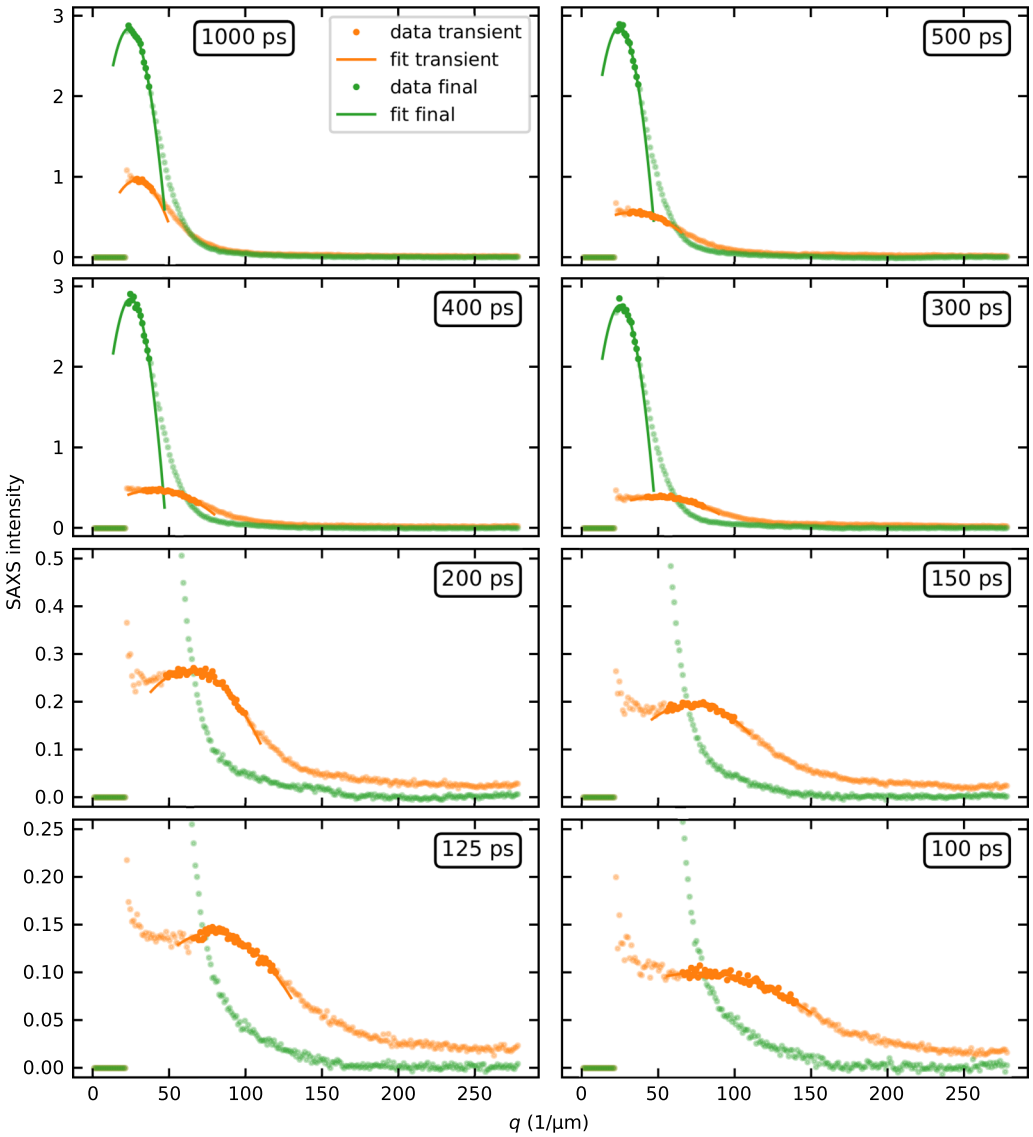


**Extended Data Fig. 9 | Fits of the peaks of the *q*-dependent intensity distributions with a local parabola.** Each panel shows the transient and final state spectra corresponding to the indicated delay. Solid lines are fits to the data. Data points considered for the fit are plotted in full contrast while all other data points are plotted with reduced contrast. The inverse of the position of the maximum of each fit, $2\pi/q_{peak}$, is the correlation length, which is a measure of the average skyrmion distance.

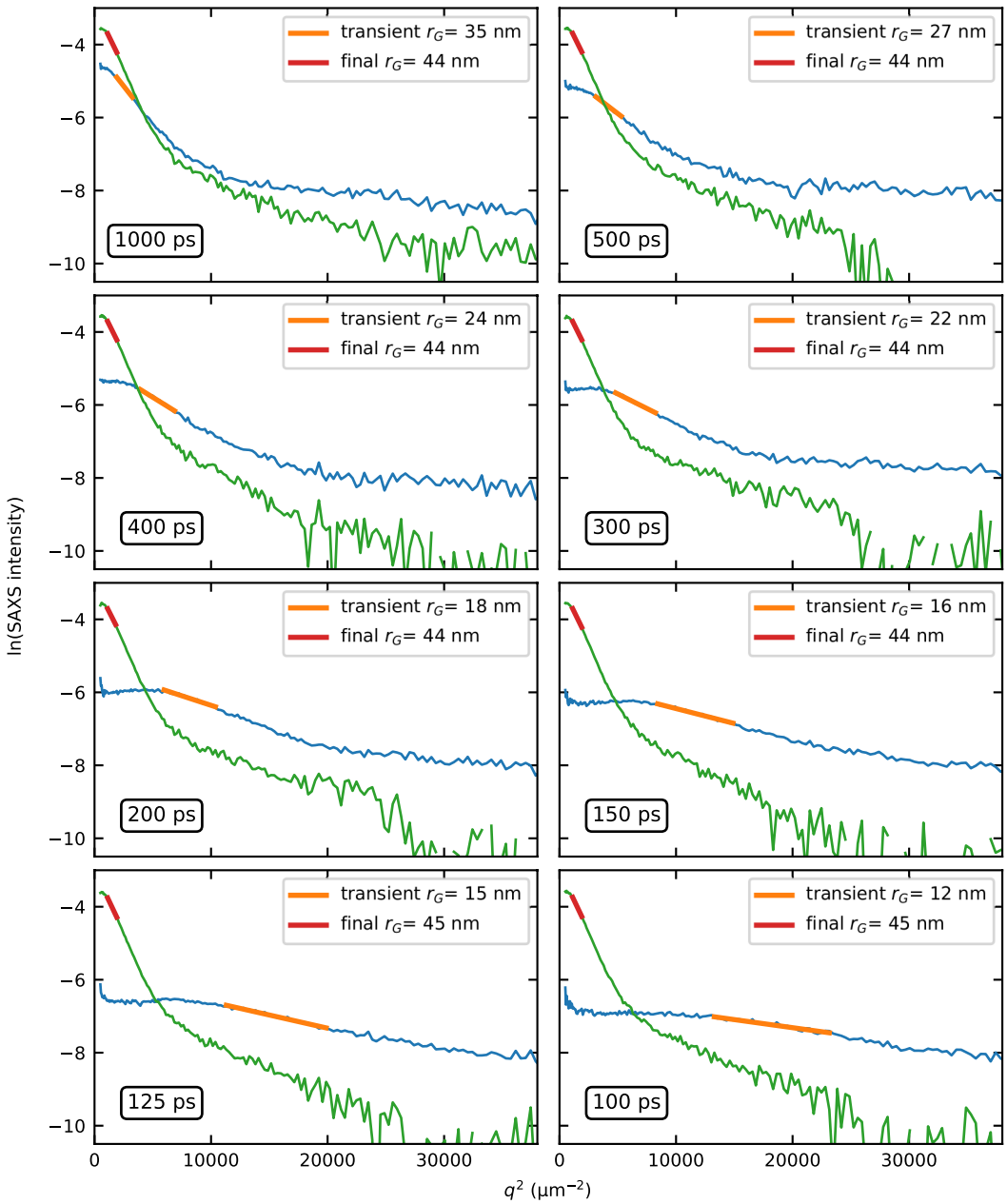


**Extended Data Fig. 10 | Natural logarithm of the scattered intensity versus the squared scattering momentum $q^2$.** The time delay is indicated in each panel. Each panel shows the background-corrected transient and final state spectra and the Guinier fits[52] of the peak shoulders. The legend provides the radii of gyration extracted from the fits.